

# Spatial-scale dependence of aerosol indirect effects over land in eastern China: A comparative analysis

Yuqin Liu<sup>1,2</sup>, Tao Lin<sup>1,2</sup>, Jiahua Zhang<sup>3</sup>, Fu Wang<sup>4</sup>, Meixia Lin<sup>1,2</sup>, Yuan Chen<sup>1,2</sup>, Yiyi Huang<sup>1,2</sup>, Hongkai Geng<sup>1,2</sup>, Xin Cao<sup>1,2</sup>, Gerrit de Leeuw<sup>5,6</sup>

1 State Key Laboratory of Regional and Urban Ecology, Institute of Urban Environment, Chinese Academy of Sciences, Xiamen 361021, China

2 Fujian Key Laboratory of Digital Technology for Territorial Space Analysis and Simulation, Fuzhou 350108, China

3 Key Laboratory of Digital Earth Sciences, The Aerospace Information Research Institute, Chinese Academy of Sciences, Beijing 100094, China

4 CMA Earth System Modeling and Prediction Centre (CEMC), Beijing 100081, China

5 Royal Netherlands Meteorological Institute (KNMI), R&D Satellite Observations, 3730AE De Bilt, The Netherlands

6 State Key Laboratory of Remote Sensing and Digital Earth & Key Laboratory of Satellite Remote Sensing of Ministry of Ecology and Environment, Aerospace Information Research Institute, Chinese Academy of Sciences, Beijing 100101, China

Correspondence to: Tao Lin ([tlin@iue.ac.cn](mailto:tlin@iue.ac.cn)); Gerrit de Leeuw ([gerrit.de.leeuw@knmi.nl](mailto:gerrit.de.leeuw@knmi.nl), ORCID: 0000-0002-1649-6333)

## Abstract

The aim of this study is to reveal patterns of the sensitivity of aerosol indirect effects to spatial scales and investigate the regulatory role of the liquid water path (LWP) in aerosol-cloud interactions over land in eastern China. Using MODIS and CALIOP satellite observations, we systematically analyzed the relationships between aerosol optical depth (AOD) and cloud properties (cloud droplet effective radius, CER; cloud droplet number concentration,  $N_d$ ) during two periods: 2008–2014 (period 1, high AOD) and 2015–2022 (period 2, decreasing AOD). The results show three distinct regimes of CER variation with LWP: a rapid growth regime ( $LWP < 55/50 \text{ g/m}^2$ ), and a decreasing regime ( $LWP = 55-135/50-100 \text{ g/m}^2$ ) (thresholds vary by period) and a slow growth regime ( $LWP > 135/100 \text{ g/m}^2$ ) (thresholds vary by period). The slow growth regime is not analyzed further due to limited data. The sensitivity of CER to AOD ( $S_{CER}$ ) exhibited a negative correlation, with stronger sensitivity in the decreasing LWP regime than in the rapid growth regime. The spatial scale (characterized by buffer size and study area) significantly modulated these sensitivities:  $|S_{CER}|$  and the positive sensitivity of  $N_d$  to

34 AOD ( $S_{Nd}$ ) both decreased with increasing spatial scale. Optimal buffer sizes range from  $6^\circ \times 6^\circ$  to  
35  $10^\circ \times 10^\circ$ : increasing with study area in period 2 but decreasing in period 1 for the decreasing LWP regime.  
36 Compared with period 1,  $|S_{CER}|$  in period 2 significantly reduced, reflecting the weakened aerosol-cloud  
37 interactions due to declining aerosol concentrations. Additionally, the optimal buffer sizes for  $S_{Nd}$  ~~were~~  
38 larger in the  $8^\circ \times 8^\circ$  and  $10^\circ \times 10^\circ$  study areas than in  $4^\circ \times 4^\circ$  and  $6^\circ \times 6^\circ$  areas. ~~This study reveals the scale-~~  
39 ~~dependence of aerosol-cloud interactions, providing critical observational support for optimizing climate~~  
40 ~~model parameterization schemes. This study reveals the scale-dependence of aerosol-cloud interactions,~~  
41 ~~providing quantitative observational constraints for optimizing scale-aware aerosol-cloud~~  
42 ~~parameterization schemes, particularly for constraining scale-dependent aerosol activation and cloud~~  
43 ~~droplet autoconversion processes.~~

44 **Keywords:** Aerosol, Cloud, Liquid water path, Scale effect, Satellite, Eastern China  
45

## 46 1 Introduction

47 Aerosol particles, depending on their chemical composition and size, can serve as cloud condensation  
48 nuclei (CCN) in liquid clouds or as ice nucleating particles (INP) in ice clouds. When CCN are activated,  
49 they can alter the microphysical properties of clouds and affect precipitation, indirectly impacting the  
50 Earth's radiative budget through aerosol-cloud interactions (aci) (Tao et al., 2012; Fan et al., 2016;  
51 Rosenfeld et al., 2019; Rao and Dey, 2020; Bellouin et al., 2020; Dagan et al., 2023). An increase in CCN  
52 concentrations results in a larger number of cloud droplets ( $N_d$ ), and if the cloud liquid water path (LWP)  
53 remains constant, it leads to a reduction in the cloud droplet effective radius (CER) (Twomey, 1974;  
54 Feingold et al., 2003). The reduced CER leads to an increased reflection of solar radiation, i.e. a higher  
55 cloud albedo, and enhances radiative forcing due to ~~aerosol-cloud interaction~~aci (RFaci). The impact of  
56 increasing aerosol particle numbers on cloud properties, while maintaining a constant LWP, is commonly  
57 known as the “Twomey” effect (Twomey, 1977; Feingold, et al., 2001; Matheson et al., 2005; Koren et  
58 al., 2005; Meskhidze and Nenes, 2010; Costantino et al., 2010; 2013). Another aspect of RFaci involves  
59 quick adjustments, which could also cause changes in other cloud characteristics due to the rise in  $N_d$  and  
60 the decrease of CER. For example, this may lead to a reduction in precipitation efficiency, causing an  
61 increase in the LWP and cloud cover. As a result, the reflection of solar radiation is intensified (Albrecht,

62 1989). These two effects of aci are often categorized as the cloud albedo effect and the cloud lifetime  
63 effect (Quaas et al., 2008).

64 Extensive research on the impact of aerosols on the microphysical properties of clouds has been  
65 conducted utilizing satellite observations (Liu et al., 2017; Jia et al., 2022), aircraft measurements (Jia et  
66 al., 2019; Zheng et al., 2024), ground-based monitoring (Sarna et al., 2016; Zheng et al., 2020), and  
67 numerical simulations (Lee et al., 2025; Li et al., 2008). Among these, satellite-based instruments have  
68 become a vital observational tool for studying aerosol-cloud interactions<sup>aci</sup> due to their wide spatial  
69 coverage and high spatiotemporal resolution. However, optical satellite sensors such as the Moderate  
70 Resolution Imaging Spectroradiometer (MODIS) cannot effectively penetrate cloud layers (King et al.,  
71 2003; Kaufman et al., 2005; Remer et al., 2005), making it difficult to directly retrieve the optical  
72 properties of aerosols underneath clouds. Currently, aerosol data are mainly obtained in cloud-free  
73 conditions as determined using cloud detection methods. This limitation results in significant spatial  
74 mismatches between aerosol and cloud properties, often requiring aggregation of satellite data over large-  
75 scale grids for statistical analysis to determine relationships between aerosol and cloud parameters. The  
76 discrepancy between this large-scale analysis and the actual process scale frequently leads to biases in  
77 quantifying aerosol indirect effects, thereby significantly increasing the uncertainty in radiative forcing  
78 estimates (Lebsock et al., 2013; Altaratz et al., 2014; Ma et al., 2015; Possner et al., 2016; Bender et al.,  
79 2018).

80 In recent years, studies based on multi-source satellite data or multi-instrument joint observations have  
81 demonstrated that aerosol particles significantly influence cloud microphysical properties (Saponaro et  
82 al., 2017; Liu et al., 2018; Pandey et al., 2020). Numerous studies have validated the existence of the  
83 Twomey effect (Jones et al., 2009; Christensen et al., 2016; Jia et al., 2019). However, also studies have  
84 been published with findings that contradict the Twomey effect, particularly over land, where an increase  
85 in aerosol optical depth (AOD) results in an increase in CER (Feingold et al., 2001; Yuan et al., 2008;  
86 Grandey and Stier, 2010; Tang et al., 2014; Wang et al., 2015; Ma et al., 2018; Jia et al., 2019; Liu et al.,  
87 2020). These inconsistent findings highlight the complexity and regional variability of aci mechanisms,  
88 and further in-depth research is needed to reveal the underlying processes.

89 Currently, researchers usually use grid methods (such as  $1^\circ \times 1^\circ$ ,  $2^\circ \times 2^\circ$ , etc.) to study the aerosol indirect  
90 effects in large areas (Bréon, 2002; Kaufman et al., 2005; Bulgin et al., 2008; Quaas et al., 2008). For

91 instance, Grandey and Stier (2010) estimated the relationship between aerosols and CER on a global  
92 scale (60°N~60°S) using multiple spatial resolutions (1°×1°, 4°×4°, 8°×8°, 15°×15°, and 60°×60°). They  
93 concluded that the sensitivity of retrieved CER to AOD generally exhibited positive values over land and  
94 negative values over oceans, and pointed out that using grids larger than 4°×4° could introduce significant  
95 errors due to the spatial variability of aerosol and cloud parameters. Additionally, the study highlighted  
96 that, when using grids larger than 4°×4° to investigate the relationship between aerosols and CER,  
97 significant errors could be introduced in calculating the aerosol indirect effect index due to the spatial  
98 variability of aerosol and cloud parameters.

99 For studies focusing on smaller regions, researchers often employ a moving window or a fixed area  
100 referred to as a buffer zone, within which the distribution of aerosol concentrations is assumed to be  
101 uniform. Spatially matched samples are constructed by averaging AOD and cloud parameters within the  
102 window or buffer zone. The choice of the window or buffer size is often arbitrary, and existing studies  
103 rarely systematically explore how the detection of aci signals is influenced by the size of the area. For  
104 example, Yuan et al. (2008) used a 100 km × 100 km moving window to calculate the mean values of  
105 AOD and cloud properties to investigate the relationship between aerosols and CER across seven global  
106 regions. Their results indicated that only two of these regions, near the coasts of the Gulf of Mexico and  
107 the South China Sea, exhibited a positive correlation between CER and AOD. Similarly, Jones et al.  
108 (2009) utilized multi-source remote sensing data and applied a point spread function to derive the mean  
109 AOD within a 20 km range, which was designed to match the native 20 km resolution of the  
110 corresponding cloud properties (cloud optical thickness, COT; LWP; CER; cloud top pressure, CTP).  
111 Their study examined the influence of aerosol types, cloud conditions, and atmospheric factors on aerosol  
112 indirect effects across six different oceanic regions globally, finding that the sensitivity of cloud  
113 properties to AOD varied substantially with regional characteristics. In addition, significant progress has  
114 been made in research utilizing observations from the Cloud-Aerosol Lidar with Orthogonal Polarization  
115 (CALIOP) data (Winker et al., 2007). For instance, Costantino et al. (2010) used CALIOP data to  
116 investigate the aerosol influence on CER in stratocumulus clouds over the coastal regions of Namibia  
117 and Angola. They performed the analysis by co-locating an aerosol index (based on AOD and the  
118 Ångström exponent) with CER within a 150 km buffer zone around CALIOP observations. They found  
119 that there was no correlation between aerosol load and CER when aerosol and cloud layers were clearly

120 separated, but a strong correlation when lidar profiles indicated mixing. Costantino et al. (2013) further  
121 analyzed the statistical relationship between aerosol concentrations and cloud physical parameters by  
122 examining aerosol and cloud properties within a 20 km buffer zone around CALIOP samples, integrating  
123 vertical profiles of aerosol and cloud data. Their statistics also clearly showed that cloud micro-physical  
124 properties were affected by aerosols when aerosol and cloud layers were mixed, decreasing the CER. It  
125 is noted that these two studies by Costantino et al. (2010, 2013) reached consistent conclusions about aci  
126 (i.e., aerosols modulate CER when layers interact), by adopting different buffer sizes (150 km vs. 20 km)  
127 to target distinct study areas. This demonstrates that the buffer size is tailored to the research objectives  
128 rather than through a systematic sensitivity analysis. Wang et al. (2015) revealed an inverse “Twomey”  
129 effect between aerosols and CER in eastern China by analyzing aerosol concentrations and CER within  
130 a 50 km buffer zone around CALIOP samples. Their results showed that larger CER was associated with  
131 high AOD, which was attributed to the feedback of microphysical processes from intense competition  
132 for vapor in the presence of high aerosol concentrations and the evaporation of smaller, less hygroscopic,  
133 droplets. Similarly, Liu et al. (2017) systematically examined the response mechanisms of warm cloud  
134 macro- and microphysical parameters to increasing AOD in the Yangtze River Delta region, also using  
135 CALIOP samples within a 50 km buffer zone. They found that the relation between cloud properties and  
136 AOD depended on the aerosol abundance, with a different behavior for low and high AOD (i.e.  $AOD < 0.35$   
137 and  $AOD > 0.35$ ). However, both Wang et al. (2015) and Liu et al. (2017) used a fixed 50 km buffer  
138 zone without justifying the choice or exploring how varying buffer sizes might alter the strength or  
139 robustness of their findings—a common limitation in regional aci studies. More recently, Liu et al. (2024)  
140 quantified the relative importance of aerosols, meteorological parameters and their interactions for cloud  
141 properties in the eastern coastal and inland regions of China, utilizing MODIS  $1^\circ \times 1^\circ$  aerosol and cloud  
142 product data. Their study confirmed that CER decreased with the increase in AOD in the moderately  
143 polluted atmosphere ( $0.1 < AOD < 0.3$ ) over the East China Sea, whereas, in contrast, CER increased  
144 with increasing AOD in the polluted atmosphere ( $AOD > 0.3$ ) over the Yangtze River Delta. These studies  
145 have provided critical scientific insights into aci at regional scales, but the lack of systematic scale  
146 sensitivity analysis—especially for varying window/buffer sizes within the same regional domain—  
147 leaves uncertainties about the generalizability of their conclusions.  
148 However, the properties and interaction processes of aerosols and clouds are spatially significantly

149 heterogeneous and scale dependent (McComiskey et al., 2009; McComiskey and Feingold, 2012; Chen  
150 et al., 2015; Glotfelty et al., 2020). McComiskey and Feingold (2012) explicitly pointed out that the  
151 “scale problem” is a major challenge in quantifying aerosol indirect effects, as the spatial scale of  
152 observation can mask or exaggerate the true interaction signals. In previous studies, the definitions of  
153 window size and buffer size have often been subjective, inadvertently introducing uncertainties into the  
154 research on aci. Although studies have explored the relationship between aerosols and CER across  
155 different observational scales, these investigations have primarily focused on larger spatial scales, leaving  
156 a gap in sensitivity analysis of aerosol indirect effects at smaller regional scales. For example, Grandey  
157 and Stier (2010) focused on global-scale grid resolutions but did not explore the scale dependence within  
158 regional domains; Wang et al. (2015) and Liu et al. (2017) used fixed buffer sizes (50 km) without  
159 investigating how varying buffer sizes affect the results. Therefore, identifying the spatial scale  
160 dependence of the aerosol indirect effect over eastern China provides observationally based coefficients.  
161 These coefficients can be used to develop regionally adapted, scale-aware parameterization schemes that  
162 better represent regional ACI characteristics,utilizing multi-source remote sensing data to explore  
163 whether and how the aerosol indirect effect depends on observational spatial scales in eastern China is  
164 of great significance for developing parameterization schemes that align with the regional characteristics  
165 of aci.

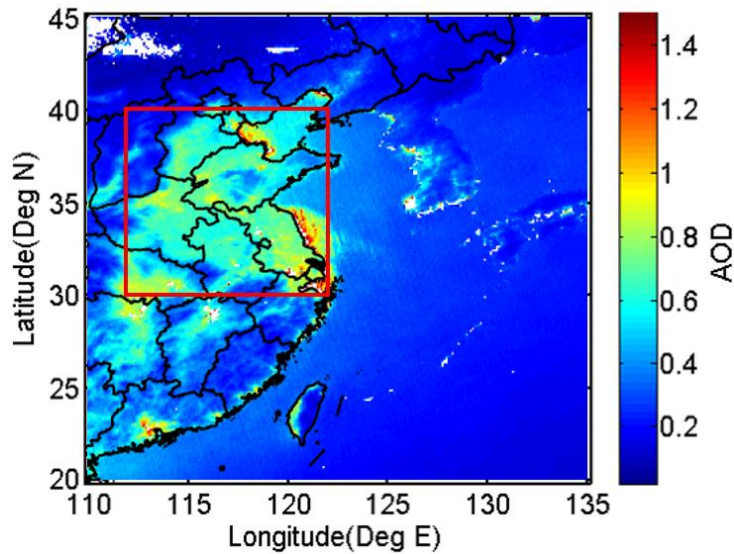
166 Aerosol properties in China have significantly changed between 2008 and 2022 due to economic  
167 development and the implementation of emission reduction policies. The AOD over China increased  
168 until 2007 to become among the highest worldwide and remained high between 2008 and 2014 with large  
169 interannual variations. The enforcement of emission reduction measures, in particular the implementation  
170 of the 2013-2017 Clean Air Action Plan, resulted in the decline of the AOD between 2014 and 2018 (de  
171 Leeuw et al., 2021; 2022; 2023) and a further decrease resulted in an AOD lower than that in 2000 (de  
172 Leeuw et al, 2023). This distinct two-period variation (high AOD vs. decreasing AOD) provides a unique  
173 opportunity to investigate how changes in aerosol loading modulate the scale dependence of aerosol  
174 indirect effects, a topic that has not been systematically addressed in previous studies. Based on these  
175 observations, in this study we conduct a comparative analysis of the sensitivity of cloud parameters (CER  
176 and  $N_d$ ) to AOD variation using data from two distinct periods: 2008-2014 (period 1, high AOD) and  
177 2015-2022 (period 2, decreasing AOD). The main objectives of this study are to: (1) reveal patterns of

178 the sensitivity of aerosol indirect effects to spatial scales by investigating how spatial scale modulates  
179 the sensitivity of CER to AOD ( $S_{CER}$ ) and the sensitivity of  $N_d$  to AOD ( $S_{Nd}$ ) over eastern China during  
180 the two periods; and (2) clarify the regulatory role of LWP in cloud-aerosol-interactionaci by examining  
181 the LWP-stratified responses of  $S_{CER}$  and  $S_{Nd}$  to spatial scale and AOD variations. The study aims to  
182 reveal the patterns of the sensitivity of aerosol indirect effects to spatial scales, provides support for  
183 optimizing parameterization schemes and accurate assessment of regional aerosol effects. This study  
184 reveals the spatial scale-dependent sensitivity of aerosol indirect effects, supporting the development of  
185 scale-adaptable parameterization modules and improved regional aerosol effect assessment under  
186 different model grid resolutions.

## 187 **2 Method**

### 188 **2.1 Study area**

189 Eastern China (30°N-40°N, 112°E-122°E; Figure 1) has undergone remarkable economic expansion over  
190 the past three decades, which was accompanied by a substantial increase in AOD. Eastern China presents  
191 a unique atmospheric laboratory due to its complex aerosol composition - featuring both anthropogenic  
192 pollutants from industrial emissions and natural mineral dust transported from Central Asian deserts,  
193 particularly during the spring (Proestakis et al., 2018; Liu et al., 2021). The multitude of sources and the  
194 persistent nature of these aerosol particles, which can remain suspended for days to weeks and be  
195 transported over long distances in the absence of precipitation (Costantino et al., 2013; Li et al., 2021;  
196 Leung et al., 2023), makes eastern China an ideal study area for investigating aci. Our research leverages  
197 satellite observations to systematically evaluate the sensitivity of cloud properties ( $S_{CER}$  and  $S_{Nd}$ ) to the  
198 AOD variation, thereby revealing the scale-sensitive patterns of aerosol indirect effects and clarifying  
199 the regulatory role of LWP in cloud-aerosol-interactionsaci over this region.



200  
 201 **Figure 1. Map of annual averaged MODIS/AQUA level 2 AOD for all years during the period from 2008 to**  
 202 **2022. The red rectangle (30°–40°N, 112°–122°E) indicates the study area.**

203 **2.2 Data used**

204 Data used in this study were acquired by the MODIS instrument aboard NASA’s Aqua satellite, which  
 205 features an extensive swath width of approximately 2300 km and comprehensive spectral coverage across  
 206 multiple bands (King et al., 2003). The satellite’s equator crossing time is 13:30 (Local time, i.e. in the  
 207 early afternoon, coinciding with optimal development conditions for continental warm cloud systems  
 208 (Wang et al., 2014; Liu et al., 2024). For aerosol characterization, we utilized the MODIS Collection 6.1  
 209 aerosol product (MOD04), generated from cloud-screened pixels with a native resolution of 500 m at  
 210 nadir and subsequently aggregated to 10 km grid cells (Remer et al., 2005; Levy et al., 2010). AOD  
 211 retrieval over land uses radiances measured at the top of the atmosphere (TOA) at wavelengths of 0.47,  
 212 0.66, and 2.13  $\mu\text{m}$  (Remer et al., 2005). The MODIS AOD (at 550 nm) Level 2 product (10 km  $\times$  10  
 213 km) has been validated against ground-based remote sensing data and the results show that 69.40% of  
 214 the MODIS AOD data fall within the expected uncertainty of  $\pm (0.05 + 15 \%)$  over land (Levy et al.,  
 215 2013). In this study, AOD larger than 1.5 was excluded from further analysis to mitigate potential  
 216 retrieval overestimation. This threshold was selected based on two key considerations: (1) Christensen  
 217 et al. (2017) used MOD06 C6 data (1 km  $\times$  1 km) and reported that “large aerosol optical depths remain  
 218 in the MODIS-observed pixels near cloud edges, due primarily to 3D effects (Varnáí and Marshak, 2009)  
 219 and the swelling of aerosols by higher relative humidity”; (2) the threshold of 1.5 aligns with widely  
 220 adopted thresholds in regional [aerosol-cloud-interactionaci](#) studies over eastern China, where high AOD

221 often coincides with complex surface conditions (e.g., urbanization, heterogeneous land cover) that  
222 exacerbate retrieval biases (Wang et al., 2015; Liu et al., 2017, 2021).

223 The cloud properties used in this study, including CER, LWP, COT, CTP, and cloud phase infrared (CPI)  
224 index, were derived from the Collection 6.1 MODIS Level 2 cloud product (MYD06) (King et al., 2003).  
225 The retrieval of these cloud characteristics utilizes six spectral channels spanning wavelengths from the  
226 visible to the near-infrared (0.66, 0.86, 1.24, 1.64, 2.12, and 3.75  $\mu\text{m}$ ) as described by King et al. (1997).  
227 Uncertainties in the MODIS C6.1 cloud parameters over land originate from instrument calibration,  
228 atmospheric correction, land surface properties, and model assumptions (Platnick et al., 2017, 2018). For  
229 COT, these include scene-dependent Level 1B data errors (1.5%–30%), land surface albedo errors  
230 ( $\pm 15\%$ ), and atmospheric correction errors ( $\pm 20\%$ ). The C6.1 algorithm addresses some prior limitations  
231 by inheriting C6’s optimized lookup table design, which reduces interpolation errors to 0.1%–0.2% for  
232 near-nadir views and corrects C5’s overestimation of thin-cloud COT (Platnick et al., 2017). CER  
233 uncertainties, stemming from solar irradiance error ( $\sim 4\%$  at 3.7  $\mu\text{m}$ ), atmospheric correction, and  
234 scattering differences, are mitigated as C6.1 retains C6’s separate multi-band reporting, thereby  
235 eliminating C5’s systematic bias (Platnick et al., 2017). LWP uncertainty is linked to COT/CER retrieval  
236 errors and cloud-phase classification accuracy; the latter is improved by C6’s voting-based phase  
237 algorithm (preserved in C6.1), which reduces misclassification over complex surfaces like vegetation  
238 and deserts (Marchant et al., 2015; Platnick et al., 2017). For CTP (1 km resolution), uncertainties from  
239 viewing angles and cloud structure are partially countered in C6.1 by assigning fill values when the 1 km  
240 retrieval fails, avoiding surface parameter defaults. For land clouds above 3 km, CTP accuracy reaches  
241  $\sim 50$  hPa (Baum et al., 2012). Finally, CPI adopts C6’s weighted voting logic (replacing C5’s sequential  
242 tree), with C6.1 maintaining an enhanced Phase Agreement Fraction against CALIOP/POLDER data,  
243 which reduces uncertainties from weak thin-cloud signals and complex land interference (Marchant et  
244 al., 2015; Platnick et al., 2017).

245 Following the methodology of Platnick et al. (2017), CER and COT measurements at 3.7  $\mu\text{m}$  were used  
246 to estimate  $N_d$  through adiabatic approximation principles (Quaas et al., 2006). Previous investigations  
247 have demonstrated that implementing filters based on cloud adiabaticity produced minimal effects on  
248  $S_{Nd}$  estimates while significantly reducing the available dataset by up to 63.00% (Gryspeerd et al., 2022).  
249 Therefore, such filtering procedures were not adopted in the current analysis. Instead,  $N_d$  calculations are

250 initially performed at the native pixel resolution (approximately 1 km) prior to spatial aggregation,  
251 thereby avoiding potential biases associated with deriving  $N_d$  from nonlinear combinations of CER and  
252 COT at coarser resolutions (Feingold et al., 2022). To maintain data quality, the analysis incorporated  
253 several quality control measures: only single-phase liquid clouds (CPI = 1) with CTP exceeding 700 hPa  
254 and LWP smaller than  $200 \text{ g m}^{-2}$  are considered, consistent with the typical atmospheric distribution of  
255 aerosols in the lower troposphere (Michibata et al., 2014). Pixels with CER values smaller than  $4 \mu\text{m}$  or  
256 COT values smaller than 4 were excluded due to increased retrieval uncertainties (Sourdeval et al., 2016).  
257 Additionally, observations were restricted to solar zenith angles  $<65.00^\circ$  and sensor zenith angles  
258  $<41.40^\circ$ . This constraint was intended to reduce the influence of well-documented biases, as elaborated  
259 in Grosvenor et al. (2018).

260 CALIPSO (Cloud-Aerosol Lidar and Infrared Pathfinder Satellite Observations) operates within the A-  
261 Train constellation alongside the Aqua satellite and other NASA Earth-observing platforms. The primary  
262 instrument aboard CALIPSO is the Cloud-Aerosol Lidar with Orthogonal Polarization (CALIOP).  
263 CALIOP is a two-wavelength, polarization-sensitive lidar specifically designed to provide high-  
264 resolution vertical profiles of aerosols and clouds on a global scale (Winker et al., 2009). The mission  
265 and its lidar instrument are described in Winker et al. (2009), and the associated Level 1 data products  
266 are detailed in Winker et al. (2010). This advanced sensor features an exceptionally narrow ground  
267 footprint of 70 m diameter for each laser pulse. The vertical resolution of CALIOP's products varies with  
268 altitude: 30 m within 0-8.2 km, 60 m between 8.2-20.2 km, and 180 m from 20.2-30.1 km, while  
269 maintaining a consistent 5 km horizontal resolution along the track direction (Liu et al., 2009).

270 The coordinated A-Train configuration ensures near-simultaneous observations (within 1-2 minutes)  
271 between MODIS/Aqua and CALIOP/CALIPSO for identical atmospheric targets (Stephens et al., 2002).  
272 This temporal synchronization guarantees data consistency when extracting coincident measurements,  
273 avoiding interferences such as aerosol diffusion and cloud evolution caused by observational time lags—  
274 an advantage unparalleled by positioning methods like random grid points and ground-based stations.  
275 For spatial compatibility, we resampled the higher-resolution MODIS cloud products (CER, LWP, and  
276  $N_d$  at 1 km native resolution) to match CALIOP's 5 km along-track scale, while directly utilizing the 5  
277 km-resolution CTP and CPI parameters. In cases where CALIOP detected aerosol presence, we  
278 computed spatial averages of MODIS aerosol and cloud retrieval products across multiple observation

279 scales (detailed in Section 2.4) centred on CALIOP targets. This approach assumes reasonable  
 280 homogeneity of aerosol properties between adjacent clear and cloudy regions (Anderson et al., 2003;  
 281 Quaas et al., 2008). Table 1 provides a comprehensive overview of the aerosol and cloud datasets  
 282 including the parameters used from each product, the resolution, and the data source, used in this study.

283  
 284  
 285  
 286  
 287  
 288  
 289  
 290  
 291  
 292  
 293  
 294  
 295  
 296

**Table 1. Aerosol and cloud products, parameters, horizontal resolutions, and their sources applied in the present study.**

<b>Product</b>	<b>Parameters</b>	<b>Horizontal resolution</b>	<b>Data source</b>
Aerosol (MYD04 Level 2 Collection 6)	Latitude	10 km	MODIS
	Longitude	10 km	
	Scan_Start_Time	10 km	
	AOD at 550 nm	10 km	
Cloud (MYD06 Level 2 Collection 6)	Latitude	5 km	
	Longitude	5 km	
	Scan_Start_Time	5 km	
	CER at 3.7 um and 2.1 um	1 km	
	LWP at 3.7 um	1 km	
	COT at 3.7 um	1 km	
	Cloud multi-layer flag	1 km	
	Cloud_Phase_Infrared_Day	5 km	
	Cloud_TOP_Pressure_Day	5 km	
	Sensor_Zenith_Day	5 km	
	Solar_Zenith_Day	5 km	
	Aerosol (05kmALay)	Latitude	
Longitude		5 km	

### 297 2.3 Calculation of sensitivities

298 Variations in aerosol loading significantly influence cloud optical properties (such as COT) and  
 299 microphysical parameters (such as CER). Under specific environmental conditions, aerosol particles can  
 300 transform into CCN or INP, a process primarily determined by their chemical composition and ambient  
 301 temperature (Bellouin et al., 2020). When these nuclei are activated, water vapor condenses on their  
 302 surfaces to form cloud droplets or ice particles. As the concentration of aerosol particles increases, the  
 303 number of CCN or INP may rise correspondingly, leading to an increase in the number of cloud droplets.  
 304 Notably, under conditions where the liquid water content in clouds remains constant (i.e., LWP), the same  
 305 amount of water vapor is distributed across more cloud droplets, resulting in a reduction in the size of  
 306 individual droplets. Specifically, as aerosol concentration increases, the CER decreases, while cloud  
 307 albedo increases. On the basis of findings of Kaufman and Fraser (1997), Feingold et al. (2001) pointed  
 308 out that the sensitivity of cloud microphysical properties (e.g., CER) to changes in the number  
 309 concentration of aerosol particles (e.g., using AOD as a measure) can be described by the following  
 310 formula:

$$311 \quad S_{\text{CER}} = \left. \frac{d \ln r_e}{d \ln \alpha} \right|_{\text{LWP}} \quad -0.33 < S < 0 \quad (1)$$

312 Where  $r_e$  represents the CER and  $\alpha$  represents the AOD. Following Andreae (2009), AOD and CCN  
 313 are correlated and AOD varies with CCN following a power law relationship. Eq. (1) describes the  
 314 relative change of CER with the relative change of the AOD for constant LWP. It is noted that this  
 315 formulation differs from that used in recent studies (e.g., Bellouin et al., 2020) where S is expressed in  
 316 terms of  $N_d$  with no restriction in LWP. The sensitivity S of CER to AOD can be determined as the slope  
 317 of a linear fit to a log-log plot of CER versus AOD. The effect of aerosols on CER is analyzed by  
 318 comparing the difference in  $S_{\text{CER}}$  and correlation coefficients between AOD and CER under different  
 319 spatial scales (Section 2.4) and LWPs (Section 3.2).

320 In this study, the variation in  $N_d$  with CCN is referred to as the susceptibility  $S_{Nd}$ . Following the method  
 321 of Gryspeerdt et al. (2023), the sensitivity,  $S_{Nd}$ , of a cloud property,  $N_d$ , to  $\alpha$  is defined here as

$$322 \quad S_{Nd} = d \ln N_d / d \ln \alpha \quad 0 < S < 1 \quad (2)$$

323 Relations between CER and  $N_d$  and AOD are determined through Eq. 1 and Eq. 2 and correlation

324 coefficients  $R$ . The significance of these relations is determined by using the student's  $t$  test, i.e. the  
325 results are statistically significant when the  $p$  value is smaller than 0.01, where  $p$  is defined as the  
326 probability of obtaining a result equal to or "more extreme" than what was actually observed.

327 This method quantifies the sensitivity of CER and  $N_d$  to AOD variations via linear regression in log-log  
328 space, using Eq. 1 and Eq. 2, respectively. Its core assumptions, uncertainties, and limitations are highly  
329 consistent: both rely on AOD as an aerosol proxy variable, assume constant cloud liquid water content  
330 and a linear sensitivity relationship, and depend on the reliability of satellite-retrieved parameters  
331 (Feingold et al., 2001; Gryspeerdt et al., 2023). However, AOD cannot distinguish aerosol size and  
332 hygroscopicity, retrieval errors are substantial in clean conditions, and linear fitting fails to capture  
333 nonlinear/non-monotonic responses. Both methods are constrained by satellite retrieval biases, limited  
334 scenario applicability (only valid for specific homogeneous clouds and aerosol types), the omission of  
335 key modulating factors (dynamical conditions, aerosol type) and feedback processes, and can only assess  
336 first-order direct effects. Reliability requires scenario constraints and uncertainty analysis; the only  
337 nuances come from the target variable (CER vs.  $N_d$ ), which do not alter the shared methodological  
338 limitations.

339

#### 340 **2.4 Research design for scale effects analysis**

341 This study was conducted at multiple spatial scales to examine the scale dependence of  $S_{CER}$  and  $S_{N_d}$  in  
342 delineating aci (Fig. 2). Here, the spatial scales are described by two parameters: study area size (the  
343 geographic scope of the analysis) and buffer size (the local spatial extent around each observation point  
344 for aggregating aerosol and cloud data). To this end, the study area was divided into four congruent square  
345 research areas all centered at the same geographical location (35°N, 117°E) over Eastern China. Hence,  
346 spatial extent varies from the whole study area as defined in Section 2.1 (30°N-40°N, 112°E-122°E) to  
347 successively smaller areas simulated by decreasing the study area in steps of 2° to 4°×4° as illustrated in  
348 Figure 2a.

349 Buffer size refers here to a circular spatial domain centered at each CALIOP-detected point in the study  
350 area where CALIOP detected the presence of aerosols. Within this circular domain, MODIS-retrieved  
351 cloud and aerosol data (AOD, CER,  $N_d$ , LWP) are spatially averaged to construct matched aerosol-cloud

352 datasets at different local scales. As previously noted, this approach relies on the assumption that aerosol  
353 properties are reasonably homogeneous between adjacent clear and cloudy regions (Anderson et al., 2003;  
354 Quaas et al., 2008), and this premise is supported by the short-range transport of aerosols (e.g., 10–300  
355 km) and the near-simultaneous observations (1–2 minutes) by MODIS and CALIOP within the A-Train  
356 constellation.

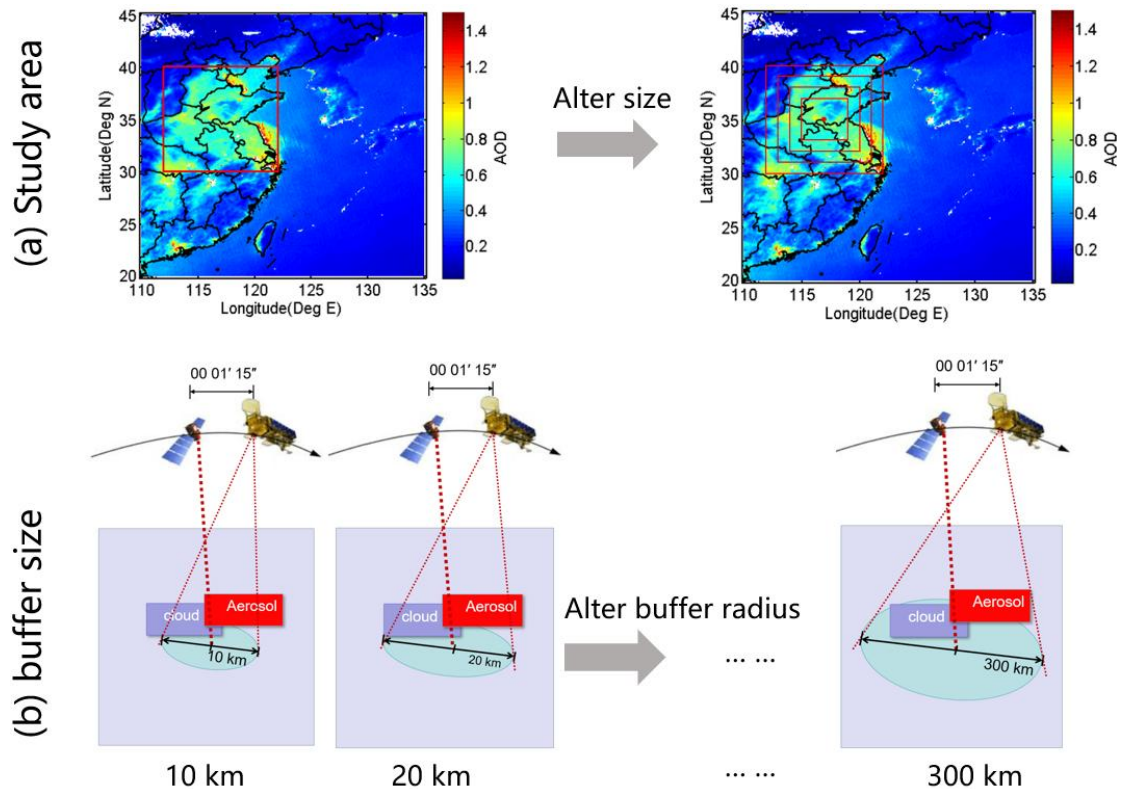
357 Buffer zones with sizes increasing from 10 to 300 km (10-km, 20-km, 30-km, 40-km, 50-km, 60-km, 70-  
358 km, 80-km, 90-km, 100-km, 120-km, 140-km, 150-km, 160-km, 180-km, 200-km, 250-km, and 300 km)

359 were determined within the whole study area by using CALIOP data. Previous observations indicate that  
360 the typical horizontal scale of cloud clusters ranges from tens to hundreds of kilometers (Zhang et al.,  
361 2024; Cai et al., 2022), supported by CloudSat/CALIPSO satellite data showing power-law distributed  
362 cloud scales (10-1000 km fitting range) covering major cloud types (Zhang et al., 2024) and regional  
363 evidence of consistent multi-season, multi-latitude cloud extents (Cai et al., 2022). Meanwhile, aerosol  
364 spatial homogeneity varies with distance: local-scale aerosols ( $\leq 50$  km) exhibit high homogeneity due  
365 to consistent sources and stable diffusion, while regional-scale aerosols ( $> 100$  km) show enhanced  
366 heterogeneity from multi-source mixing and atmospheric transport (Hassan et al., 2024; Mohebalhojeh  
367 et al., 2026). Thus, the 10–300 km buffer range covers both cloud characteristic scales and the aerosol  
368 homogeneity transition range, ensuring that MODIS data averaging effectively captures cloud-aerosol  
369 coupling. This range avoids insufficient MODIS pixel coverage due to excessively small buffer sizes  
370 ( $< 10$  km). It also prevents conflation between regional meteorological variations and local aci signals  
371 arising from overly large buffer sizes ( $> 300$  km), as synoptic-scale circulation and other regional  
372 meteorological changes may interfere with local aci signals (Quaas et al., 2010). Meanwhile, this range  
373 aligns with the 50 – 150 km buffer sizes widely adopted in regional aci studies (Wang et al., 2015; Liu et  
374 al., 2017; 2024), enabling cross-validation of results and ensuring that MODIS data averaging effectively  
375 captures cloud-aerosol-coupling.

376 MODIS-retrieved cloud and aerosol data were averaged over a buffer area around each CALIOP data  
377 point with a radius varying from 10-km to 300 km. Thus, a dataset including aerosol and cloud properties  
378 was constructed with different buffer sizes. The effect of buffer size on the sensitivity of CER and  $N_d$  to  
379 variations in AOD was determined in each study area varying from  $4^\circ \times 4^\circ$  to  $10^\circ \times 10^\circ$ . To this end, for  
380 each buffer size, the averaged AOD and cloud parameters were paired to calculate the sensitivities  $S_{CER}$

381 (Eq. 1) and  $S_{Nd}$  (Eq. 2), as well as their correlation coefficients (R) between cloud properties (e.g., CER,  
382  $N_d$ ) and AOD. The optimal buffer size for each study area is defined as the one maximizing the R. This  
383 definition is adopted based on two core considerations. Firstly, it aligns with the statistical principle that  
384 a higher R value indicates a stronger linear correlation between the two variables in ~~the~~-log-log space,  
385 minimizing the interference of random noise and non-aerosol confounding factors on the sensitivity  
386 estimation (Quaas et al., 2006; Gryspeerd et al., 2022). This ensures that the derived  $S_{CER}$  can reliably  
387 reflect the intrinsic relationship between aerosol loading and cloud droplet effective radius, rather than  
388 spurious correlations caused by inappropriate spatial scales. Secondly, this definition also facilitates  
389 comparability with existing literature, as it aligns with the methodological framework of satellite-based  
390 ~~aerosol-cloud-interactionaci~~ studies (Saponaro et al., 2017; Liu et al., 2021). In these studies, the optimal  
391 spatial scale is typically identified by maximizing the statistical robustness of variable correlations.

392 The dataset was used to study the characteristics of aerosol indirect effects as function of buffer size and  
393 study area, for two different periods: one with a high aerosol content (2008-2014) and another one with  
394 a decreasing aerosol content (2015-2022). ~~This approach enabled the determination of the optimal buffer~~  
395 ~~size for aerosol indirect effects as function of the size of the study area, ultimately leading to the~~  
396 ~~development of a parameterization scheme for aerosol indirect effects for observations with different~~  
397 ~~spatial resolution and different sizes of the study area over eastern China. This approach determined the~~  
398 ~~optimal buffer size for aerosol indirect effect estimations as a function of study domain size, providing~~  
399 ~~key observational constraints for constructing scale-adaptive parameterization frameworks suitable for~~  
400 ~~different domain sizes over eastern China.~~



401

402 **Figure 2. (a) Schematic diagram of study area and buffer size patterns applied in this study. (b) scheme of**  
 403 **CALIPSO-MODIS coincidence methodology. When CALIPSO detects the presence of aerosol and cloud fields,**  
 404 **we look for MODIS retrievals within a buffer size from the CALIPSO target. The temporal coincidence is**  
 405 **insured by the coordinated satellite orbits.**

### 406 3 Results

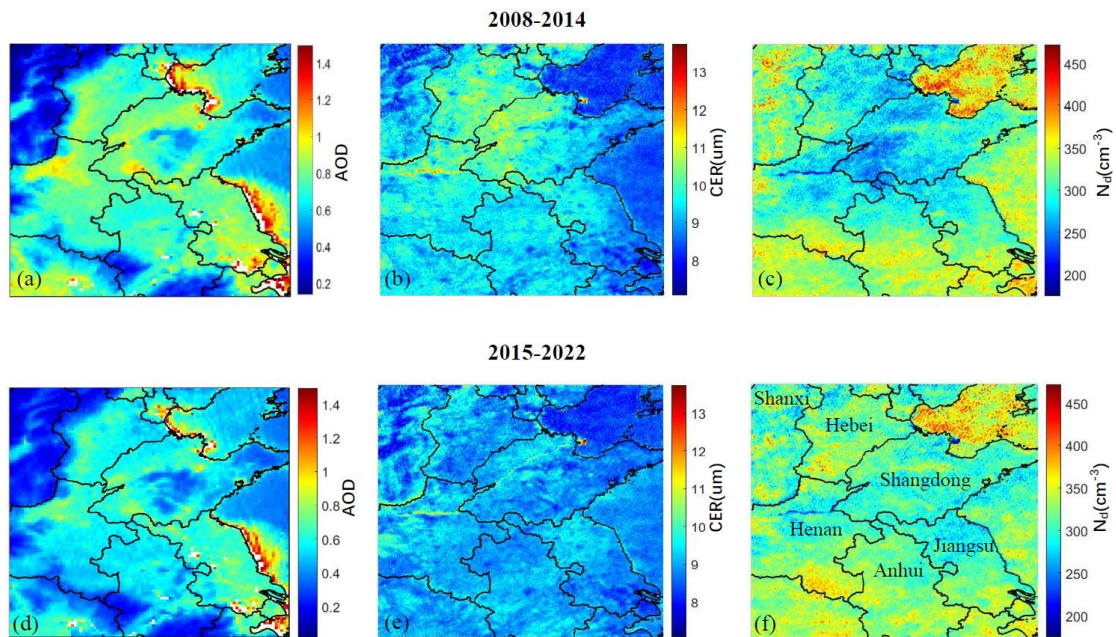
#### 407 3.1 Spatial variations of aerosol and cloud parameters

408 Figure 3 illustrates the spatial distributions of AOD and cloud properties (CER and  $N_d$ ) across the study  
 409 region, averaged for the periods 2008-2014 and 2015-2022. The AOD spatial patterns (Fig. 3a,d) show  
 410 similar spatial distributions during both periods, but with notably reduced values during the latter.  
 411 Pronounced spatial gradients in AOD are evident during both periods. The lowest AOD values occur over  
 412 the mountainous regions of Shanxi province in the northwest, while elevated concentrations appear in  
 413 the southeastern areas encompassing the Hebei and Shandong provinces. This geographical contrast  
 414 arises from the mountain ranges that demarcate the heavily industrialized, densely populated North China  
 415 Plain (NCP) in the east - characterized by substantial anthropogenic emissions - from the relatively  
 416 cleaner pristine western regions. Under prevailing southeasterly wind conditions, these topographic  
 417 barriers effectively block transport of atmospheric pollutants which accumulate along their windward

418 slopes (Sundström et al., 2012). The concentration of heavy industries and power generation facilities in  
 419 the NCP are primarily responsible for the observed high AOD concentrations, together with  
 420 meteorological and geographical conditions. Additionally, lower AOD values appear in southern Anhui  
 421 and central Shandong relative to the surrounding regions.

422 The CER spatial distributions (Fig. 3b,e) reveal distinct differences between the two periods. During  
 423 2008-2014, larger cloud droplets predominated in the northern sectors, particularly throughout Hebei and  
 424 western Shandong. Notably, the spatial correspondence between AOD and CER maxima aligns with the  
 425 anti-Twomey effect, suggesting that the high aerosol loading promoted cloud droplet growth rather than  
 426 suppression - consistent with findings from Wang et al. (2014) and Liu et al. (2018). The 2015-2022  
 427 period shows markedly reduced CER values (typically  $<10 \mu\text{m}$ ) with enhanced spatial homogeneity.

428 Similarly,  $N_d$  exhibits contrasting spatial patterns between the two periods (Fig. 3c,f). The earlier  
 429 timeframe shows depressed  $N_d$  values in central regions surrounded by elevated concentrations  
 430 peripherally. This pattern reverses during 2015-2022, with increases of  $N_d$  in the central area  
 431 accompanied by overall reduction of the cloud droplet concentrations in the surrounding regions.

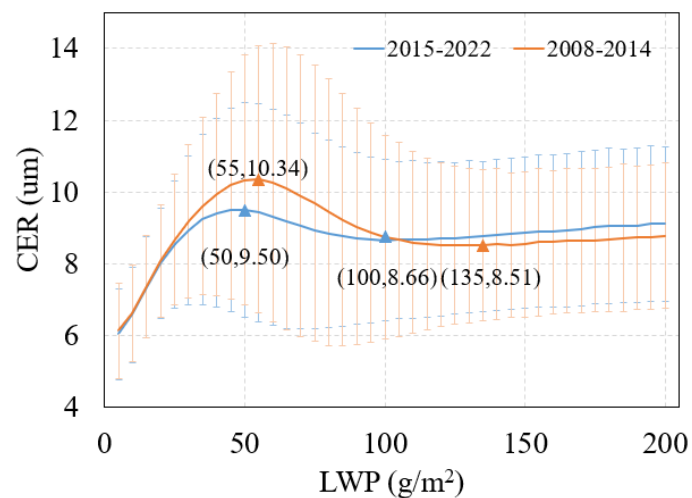


432  
 433 **Figure 3. Spatial distributions of AOD (a, d), CER (b, e) and  $N_d$  (c, f), averaged over the years 2008-2014 (top**  
 434 **row) and 2015-2022 (bottom row) over the study area. The lines are provincial borders and the names of**  
 435 **provinces mentioned in the text are indicated in Fig. (f).**

### 436 3.2 Sensitivity of CER to AOD stratified by LWP

437 Before analyzing the influence of AOD on CER, the relationship between CER and LWP should be

438 investigated. The values of the LWP were divided into 40 subsets with a width of  $5 \text{ g/m}^2$ , and then the  
 439 average value of CER in each subset was calculated and plotted as function of LWP (Figure 4).  
 440 The variation of CER with LWP shows three regimes. For LWP smaller than  $55 \text{ g/m}^2$  (period 1) or  $50$   
 441  $\text{g/m}^2$  (period 2), CER increased rapidly with the increase of LWP. This first LWP regime is referred to as  
 442 a rapid growth regime (LWP1). The second LWP regime, referred to as a decreasing regime (LWP2),  
 443 applies to the LWP range from  $55 \text{ g/m}^2$  to  $135 \text{ g/m}^2$  (period 1) or  $50\text{-}100 \text{ g/m}^2$  (period 2) and CER  
 444 decreased with the increase of LWP. When LWP was greater than  $135 \text{ g/m}^2$  (period 1) or  $100 \text{ g/m}^2$  (period  
 445 2), CER increased with increasing LWP but at a much slower rate than during the first regime; the third  
 446 LWP regime is therefore referred to as a slow growth regime (LWP3). These results show that CER is  
 447 very sensitive to the changes in LWP, which is consistent with the study of Liu et al. (2021). Specifically,  
 448 CER exhibited a three-stage variation with LWP: rapid growth when  $\text{LWP} < 50 \text{ g/m}^2$  (with the fastest  
 449 change rate), a stable state during  $50\text{-}150 \text{ g/m}^2$ , and slow growth when  $\text{LWP} > 150 \text{ g/m}^2$  (at a rate much  
 450 lower than the first stage). This highlighted the necessity of fixing LWP conditions to accurately  
 451 investigate the impact of AOD on CER. To separate the effects of changing LWP on CER from those of  
 452 changing AOD on CER, relations between CER and AOD were evaluated for constant LWP  
 453 (McComiskey et al., 2012), for each of the three regimes mentioned above, by using double-logarithmic  
 454 plots of AOD versus CER. The number of CER observations in the third regime is too small to achieve  
 455 statistically meaningful results, therefore the sensitivity of CER to AOD was only analyzed for the rapid  
 456 growth and decreasing CER regimes.



457  
 458 **Figure 4. Variation of CER with LWP over the study area. Here all CER data were averaged in LWP bins,**  
 459 **from 0 to  $200 \text{ g/m}^2$  with a width of  $5 \text{ g/m}^2$ . The red line is a fit to the data during 2008-2014 and the blue line**  
 460 **for the data during 2015-2022. The numbers in parentheses indicate the (LWP, CER) values for the inflection**

461 points between the regimes. The error bars (the vertical lines) denote the standard deviations, indicating the  
462 variability of CER around the average at each LWP value.

### 463 3.2.1 Rapid CER growth regime

464 For the first LWP regime, the  $S_{CER}$  is negative (as shown in Figure 5). This aligns with the Twomey effect  
465 (Twomey, 1977): an increase in aerosols raises the number of CCN, and with constant LWP, less water  
466 vapor is available per cloud droplet, reducing CER, increasing cloud albedo, and ultimately cooling the  
467 atmosphere. This indicates that, in the rapid growth regime, the interaction between AOD and CER in  
468 the target region is in agreement with the Twomey effect. The data in Figure 5a show that during period  
469 1,  $S_{CER}$  varies with buffer size and that the variations are different for different study areas. The value of  
470  $|S_{CER}|$  is smallest for the largest study area ( $10^\circ \times 10^\circ$ ) and decreases with buffer size to a minimum for  
471 buffer size of 150 km and then increases. For the smallest study area ( $4^\circ \times 4^\circ$ ), the sensitivity exhibits a  
472 much stronger negative correlation, with its magnitude decreasing as the buffer size expands, especially  
473 for  $50 \text{ km} < \text{buffer size} < 100 \text{ km}$ . For the 2 intermediate study areas, the sensitivities are initially similar  
474 (except for the smallest buffer size) and diverge for  $\text{buffer size} > 100 \text{ km}$ . The data show that the value of  
475  $|S_{CER}|$  overall becomes smaller as study area increases. The decrease of  $|S_{CER}|$  with increasing study area  
476 is mechanistically tied to scale-dependent aerosol indirect effect theory and meteorological confounding  
477 (Quaas et al., 2009; McComiskey & Feingold, 2012). The correlation coefficients  $R$  (bottom of Figure 5  
478 a) are similar for all four study areas at small buffer sizes, increase fast with buffer size to a maximum  
479 for a buffer size of about 50 km and then decrease and diverge. The largest decrease is observed for the  
480 study area of  $10^\circ \times 10^\circ$ . In this study, the optimal scale for each study area is indicated in Figure 5 with a  
481 red solid square. A plot of the optimal scale versus the size of the study area in Figure 6 (curve LWP1-  
482 period1) shows that, as the study area size increased from  $6^\circ \times 6^\circ$  to  $10^\circ \times 10^\circ$ , the optimal scale decreased  
483 from 100 km to 30 km.

484 As compared with period 1, in period 2 (Figure 5b) the value of the  $|S_{CER}|$  also decreases as the buffer  
485 size increases. However, the scale sensitivity analysis for period 2 revealed two distinct characteristics  
486 different from period 1: (1) the four  $S_{CER}$  curves for different study areas are much closer than during  
487 period 1; (2) with the exception of the study area of  $10^\circ \times 10^\circ$ , the values of the  $|S_{CER}|$  for the other three  
488 study areas are significantly reduced (closer to zero), indicating a corresponding weakening of aerosol-  
489 cloud-interaction intensity against the background of decreased aerosol concentrations. Particularly

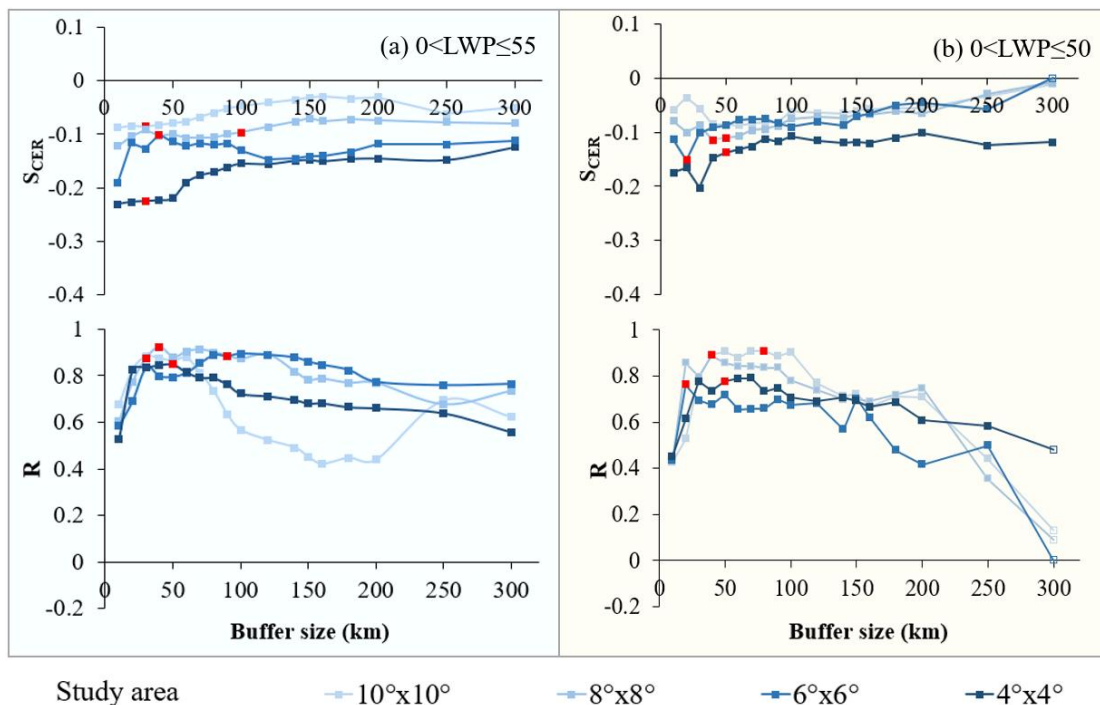
490 noteworthy is that during period 1, the R values for the  $10^\circ \times 10^\circ$  study area showed a sharp declining  
491 trend when the buffer size exceeds 60 km, while in period 2 this happened for buffer size larger than  
492 110 km and the R value curves for all study areas significantly expanded their high-value ranges. Also  
493 for period 2, the R values for the study areas of  $10^\circ \times 10^\circ$  and  $8^\circ \times 8^\circ$  are very similar, in contrast to period  
494 1 when only the R values for the study areas of  $10^\circ \times 10^\circ$  decreases fast. Across different study areas, the  
495 optimal scale (Curve LWP1-peirod2) shows a behavior opposite to that during period 1: as the study area  
496 size increases from  $6^\circ \times 6^\circ$  to  $10^\circ \times 10^\circ$ , the optimal scale increases from 20 km to 80 km. It is noted  
497 that for a study area of  $4^\circ \times 4^\circ$  the optimal scale is 50 km in both periods. For the first LWP regime,  
498  $S_{CER}$  estimates and correlation coefficients R by period and optimal buffer size across  $4^\circ \times 4^\circ$  to  $10^\circ \times 10^\circ$   
499 study areas are given in Appendix A1.

### 500 3.2.2 Decreasing CER regime

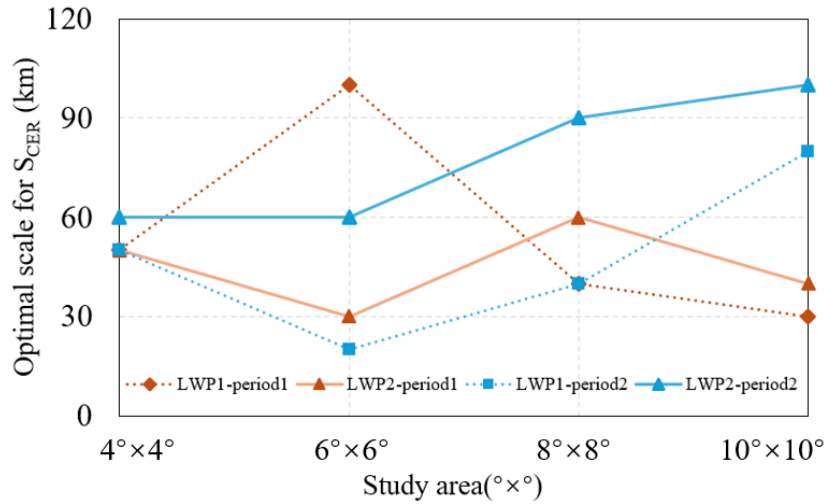
501 During the second LWP regime (Figure 7), the AOD and CER is also negatively correlated ( $S_{CER} < 0$ )  
502 during both periods, but the values of  $S_{CER}$  vary stronger with the size of study area: the curve dispersion  
503 increases in the second LWP regime, the values of  $|S_{CER}|$  are larger overall, and the relatively concentrated  
504 trend in the period 1 shifts to more scattered fluctuations in the period 2. During period 1, for the largest  
505 ( $10^\circ \times 10^\circ$ ) study area: the value of  $|S_{CER}|$  (Figure 7a) decreases with increasing buffer size, nearing zero  
506 at ~150 km, briefly turning slightly positive, then slowly falling below zero by 220 km. For the three  
507 smaller study areas, the  $S_{CER}$  values are all negative and  $|S_{CER}|$  overall decreased with increasing  
508 buffer size. Through the sensitivity of  $S_{CER}$  to buffer size across varying study areas during period 1, the  
509 value of  $|S_{CER}|$  for a given buffer size becomes smaller with increasing study area size. Additionally,  
510 across all study areas,  $|S_{CER}|$  initially increases with the increase of the buffer size, then decreases, and  
511 gradually stabilizes thereafter. The data in Figure 6 (Curve LWP2-peirod1), show that, the optimal size  
512 varies between 30 km and 60 km with no clear dependence on the size of the study area.

513 Compared with period 1, the value of  $|S_{CER}|$  in period 2 (Figure 7b) also decreased overall with increasing  
514 buffer size, and at the same buffer size,  $|S_{CER}|$  decreased as study area increased. However, the scale  
515 sensitivity analysis for period 2 revealed two distinct characteristics: (1) the four curves for different  
516 study areas were closer than during period 1; (2) the  $|S_{CER}|$  for the study area of  $10^\circ \times 10^\circ$  was overall  
517 larger, while the values of the  $S_{CER}$  curves for the study areas of  $4^\circ \times 4^\circ$  and  $6^\circ \times 6^\circ$  were significantly

518 reduced and that for the study area of  $8^\circ \times 8^\circ$  was slightly reduced. The reduction may be attributed to  
 519 weakened aerosol-cloud interactions resulting from decreased regional aerosol concentrations (Jia et  
 520 al., 2022; Li et al., 2024; Zhao et al., 2025). The variation of the optimal scale (Curve LWP2-period2)  
 521 with the size of the study area is similar to that during period 1 in the rapid growth LWP regime: as the  
 522 study area size increased from  $6^\circ \times 6^\circ$  to  $10^\circ \times 10^\circ$ , the optimal scale increased from 60 km to 100 km.  
 523 For the second LWP regime,  $S_{CER}$  estimates and correlation coefficients R between CER and AOD by  
 524 period and optimal buffer size across  $4^\circ \times 4^\circ$  to  $10^\circ \times 10^\circ$  study areas are given in Appendix A1.  
 525 Through comparative analysis of  $S_{CER}$  data distribution across different LWP regimes under different  
 526 aerosol conditions (i.e. high AOD and decreasing AOD), we found that the  $|S_{CER}|$  in the second LWP  
 527 regime was significantly larger than that in first LWP regime except for the study area of  $10^\circ \times 10^\circ$  for  
 528 buffer size  $>100$  m, where  $S_{CER}$  curves corresponding to different study areas showed greater dispersion.  
 529 This pattern highlights the dominant role of LWP in regulating aerosol-cloud interaction sensitivity,  
 530 with AOD variations further modulating the magnitude of such differences. Sample sizes of CER and  
 531 AOD for the first LWP regime across both study periods, all buffer sizes and study areas, are presented  
 532 in Appendices A3–A6.

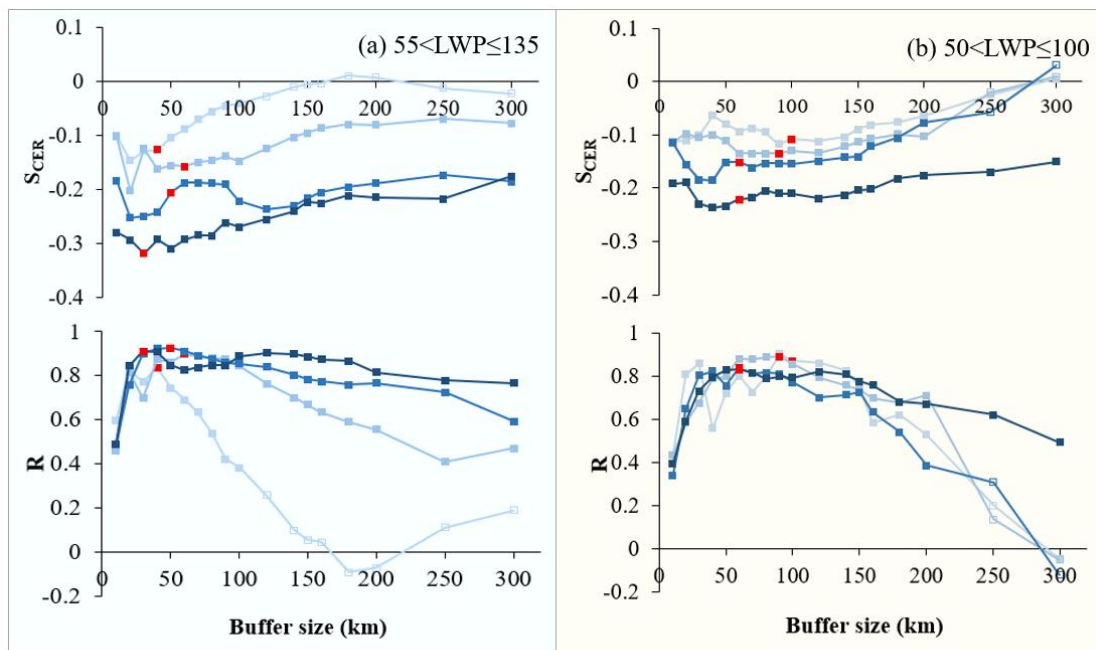


533 Study area  $10^\circ \times 10^\circ$   $8^\circ \times 8^\circ$   $6^\circ \times 6^\circ$   $4^\circ \times 4^\circ$   
 534 Figure 5. Variation of  $S_{CER}$  (top) and correlation coefficient R (bottom) with buffer size for different study  
 535 areas (see legend at the bottom) for (a) the LWP regime with  $0 < LWP \leq 55$   $g/m^2$  over the years of 2008–2014 and  
 536 (b) the LWP regime with  $0 < LWP \leq 50$   $g/m^2$  over the years of 2015–2022. Filled squares indicate that the results  
 537 are significant at the 0.01 level and open squares indicate that the results are not statistically significant. The  
 538 red solid squares indicate the optimal buffer sizes for each study area, as shown in the Appendix A1.



539  
540  
541  
542  
543  
544

Figure 6. Relationship between optimal scale for SCER and the size of the study area. Here LWP1-period1 and LWP2-period1 indicate the optimal scale in period 2008-2014 for the first LWP regime and that for the second LWP regime, respectively. LWP1-period2 and LWP2-period2 indicate the optimal scale in period 2015-2022 for the first LWP regime and that for the second LWP regime, respectively.



Study area      10°x10°      8°x8°      6°x6°      4°x4°

545  
546  
547  
548  
549  
550  
551

Figure 7. Variation of SCER (top) and correlation coefficient R (bottom) with buffer size for different study areas (see legend at the bottom) for (a) the LWP regime with  $55 < LWP \leq 135$  g/m<sup>2</sup> over the years of 2008-2014 and (b) the LWP regime with  $50 < LWP \leq 100$  g/m<sup>2</sup> over the years of 2015-2022. The filled squares indicates that the results are significant at the 0.01 level and the open squares indicates that the results are not statistically significant. The red solid squares indicate the optimal buffer sizes for each study area, as shown in the Appendix A1.

### 552 3.3 Sensitivity of $N_d$ to AOD

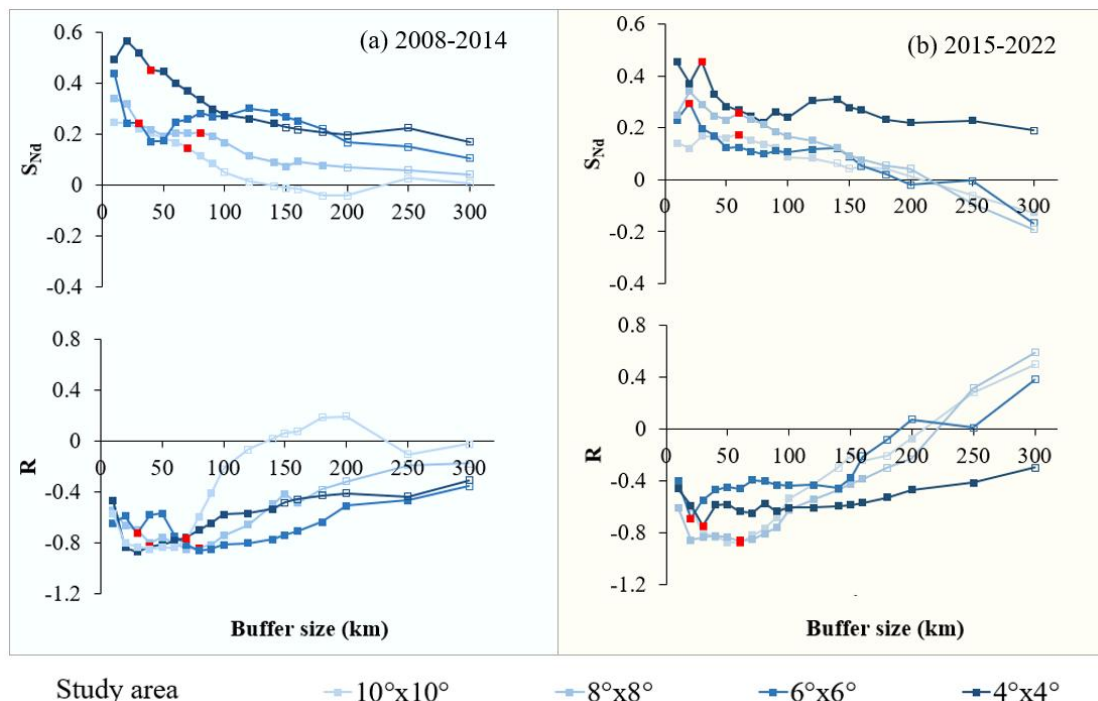
553 Eq. (2) shows that the value of the sensitivity of  $N_d$  to AOD is determined by the slope of a linear fit to a  
554 log-log plot of  $N_d$  versus AOD. To investigate  $S_{N_d}$ , we used correlated data pairs for each of the 7 years  
555 during periods 1 and 2, binned the data in AOD intervals with a bin width of 0.02, and the  $N_d$  data in  
556 each AOD bin were averaged. The sensitivity  $S_{N_d}$  is defined as the slope of a linear fit to a log-log plot  
557 of  $S_{N_d}$  versus AOD (Eq. 2). For each period, we binned the data into AOD intervals of 0.02 and averaged  
558  $N_d$  within each bin. The variation of  $S_{N_d}$  with buffer size for different study areas over the target region  
559 is presented in Figure 8. Figure 8 shows the variation of  $S_{N_d}$  with buffer size for different study areas, for  
560 both periods. The data in Figure 8 show that, in contrast to  $S_{CER}$ ,  $S_{N_d}$  is predominantly positive ( $p < 0.01$ )  
561 during in both periods, and decreases with increasing buffer size. During period 1 (2008–2014, high  
562 AOD),  $S_{N_d}$  for the study area of  $6^\circ \times 6^\circ$  study area decreases rapidly to a minimum at buffer sizes of 40–  
563 50 km, then the  $S_{N_d}$  initially decreases very fast to a minimum at a buffer size of 40 to 50 km, followed  
564 by an increase to a maximum at a buffer size of 120 km. For buffer size  $\geq 120$  km, the two smallest  
565 study areas ( $4^\circ \times 4^\circ$  and  $6^\circ \times 6^\circ$ ) yield similar  $S_{N_d}$  values, which are similar for the two smallest study  
566 areas and substantially larger than those for the two larger study areas ( $8^\circ \times 8^\circ$  and  $10^\circ \times 10^\circ$ ). During  
567 period 2 (2015–2022, decreasing AOD), we can see an initial increase of  $S_{N_d}$  for the study area of  $6^\circ \times 6^\circ$   
568 and  $8^\circ \times 8^\circ$ , and variation of  $S_{N_d}$  for the study area of  $10^\circ \times 10^\circ$  and  $4^\circ \times 4^\circ$ . After that, the  $S_{N_d}$  for the study  
569 area of  $4^\circ \times 4^\circ$  and  $6^\circ \times 6^\circ$  decreases very fast rapidly to a minimum for a buffer size of 80 km, followed by  
570 an increase to a maximum for a buffer size of 140 km. The variation of  $R$  with buffer size for each of the  
571 two periods shows that the optimal buffer sizes are larger when the study area is larger. Specifically, these  
572 optimal sizes in the  $8^\circ \times 8^\circ$  and  $10^\circ \times 10^\circ$  study areas are larger than those in the  $4^\circ \times 4^\circ$  and  $6^\circ \times 6^\circ$  areas  
573 (Figure 9).

574 The optimal buffer sizes (maximizing  $R$ ) are larger for the  $8^\circ \times 8^\circ$  and  $10^\circ \times 10^\circ$  study areas than for the  
575  $8^\circ \times 8^\circ$  and  $10^\circ \times 10^\circ$  areas (Fig. 9), reflecting different characteristics in aerosol-cloud interactions and  
576 characteristics in different under varying AOD conditions. The estimates of  $S_{N_d}$  and correlation  
577 coefficients  $R$  between  $N_d$  and AOD, stratified by optimal buffer size, for study areas ranging from  $4^\circ \times 4^\circ$   
578 to  $10^\circ \times 10^\circ$  during the two periods are presented in the Appendix A2.

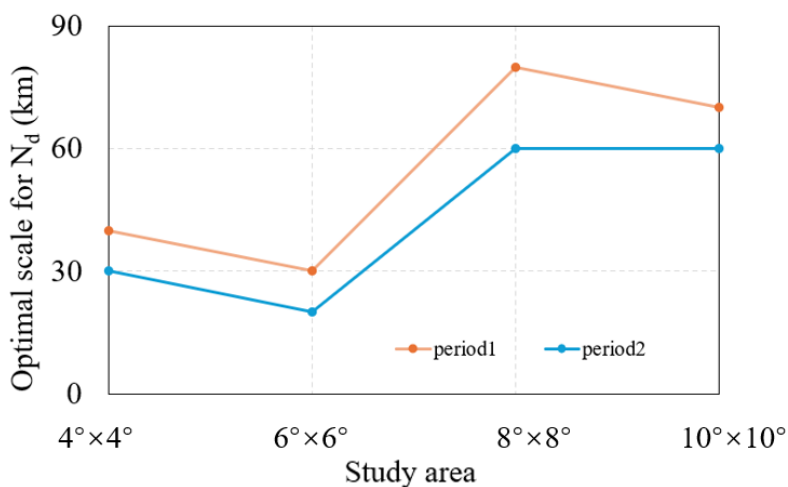
579 It is noted that  $S_{CER}$  and  $N_d$  exhibit distinct anomalies in large buffer zones, which may be associated  
580 with key factors including aerosol distribution, meteorological heterogeneity, cloud type transitions, and

581 ~~satellite retrieval limitations. Expanding the study area inevitably increases spatial heterogeneity in~~  
582 ~~aerosol loading, meteorology, and cloud type, while also introducing larger satellite retrieval~~  
583 ~~uncertainties. This spatial mixing blends clean and polluted air masses, thereby introducing a statistical~~  
584 ~~dilution effect on the estimated  $S_{Nd}$ . Therefore, the decrease in  $S_{Nd}$  with increasing study area size (Fig. 8)~~  
585 ~~reflects not only a genuine weakening of aerosol-cloud interactions but also the combined effects of~~  
586 ~~meteorological confounding, cloud regime transitions, and retrieval limitations. It is noted that  $S_{CER}$  and~~  
587  ~~$S_{Nd}$  exhibit distinct anomalies in large buffer zones, which may be associated with all these factors.~~  
588 ~~The chemical composition of aerosols, which directly affects AOD and CCN activation efficiency,~~  
589 ~~underwent significant changes between the two periods due to policy interventions. During 2008–2014,~~  
590 ~~aerosols over eastern China were dominated by sulfate, which accounted for 30%–40% of the  $PM_{2.5}$  mass~~  
591 ~~(Huang et al., 2014; Zheng et al., 2018). Given the strong hygroscopicity of sulfate-dominated aerosols~~  
592 ~~(Zhang et al., 2012; Liu et al., 2023), their CCN activation efficiency was likely high, which may have~~  
593 ~~provided a critical physical basis for the aerosol-cloud indirect effect (Lee et al., 2009). In the period of~~  
594 ~~2015–2022, driven by policies such as the Air Pollution Prevention and Control Action Plan (Zheng et~~  
595 ~~al., 2018), the chemical composition of aerosols underwent a structural transition. Specifically, the mass~~  
596 ~~fraction of sulfate dropped sharply to 15%–25% with an absolute concentration reduction of more than~~  
597 ~~50%, while the relative proportions of nitrate, carbonaceous aerosols (i.e., organic carbon (OC) and black~~  
598 ~~carbon (BC)), and secondary organic aerosols (SOA) showed an increasing trend (Huang et al., 2014;~~  
599 ~~Zheng et al., 2018). As these components generally exhibit weaker hygroscopicity compared with sulfate~~  
600 ~~(Zhang et al., 2012; Liu et al., 2023), such a compositional shift might have led to a decrease in CCN~~  
601 ~~activation efficiency under the same AOD conditions, thereby potentially weakening the sensitivity of~~  
602 ~~cloud droplet number concentration to AOD and altering the intensity and mode of aerosol-cloud~~  
603 ~~interactions to a certain extent (Lee et al., 2009).~~  
604 ~~Changes in aerosol chemical composition between the two periods may also modulate  $S_{Nd}$ . During 2008–~~  
605 ~~2014, aerosols over eastern China were dominated by sulfate (30%–40% of  $PM_{2.5}$  mass; Huang et al.,~~  
606 ~~2014; Zheng et al., 2018). Given the strong hygroscopicity of sulfate-dominated aerosols (Zhang et al.,~~  
607 ~~2012; Liu et al., 2023), their CCN activation efficiency was likely high, providing a favorable physical~~  
608 ~~basis for aci (Lee et al., 2009). In contrast, during 2015–2022, policy interventions (e.g., the Air Pollution~~  
609 ~~Prevention and Control Action Plan; Zheng et al., 2018) drove a structural transition: the sulfate mass~~

610 fraction dropped sharply to 15%–25% (an absolute reduction of >50%), while less hygroscopic  
 611 components (nitrate, carbonaceous aerosols, and secondary organic aerosols) increased in relative  
 612 proportion (Huang et al., 2014; Zheng et al., 2018). As these components generally exhibit weaker  
 613 hygroscopicity compared with sulfate (Zhang et al., 2012; Liu et al., 2023), this compositional shift may  
 614 have reduced CCN activation efficiency under the same AOD, thereby weakening the sensitivity of  $N_d$   
 615 to AOD and altering aci intensity (Lee et al., 2009).



616 Study area  $10^{\circ} \times 10^{\circ}$   $8^{\circ} \times 8^{\circ}$   $6^{\circ} \times 6^{\circ}$   $4^{\circ} \times 4^{\circ}$   
 617 Figure 8. Variation of  $S_{Nd}$  (top) and correlation coefficient  $R$  (bottom) with buffer size for different study areas  
 618 (see legend at the bottom) for the LWP regime with  $0 < LWP \leq 200 \text{ g/m}^2$  over the years of 2008-2014 (a) and  
 619 2015-2022 (b). The filled squares indicates that the results are significant at the 0.01 level and the open  
 620 squares indicates that the results are not statistically significant. The red solid squares indicates the optimal  
 621 buffer size for each study area, as shown in the Appendix A2.



622  
 623 Figure 9. Relationship between optimal scale for  $N_d$  and the size of the study area. Here period1 and period2

624 indicate the optimal scale in period 2008-2014 and the optimal scale in period 2015-2022, respectively.

## 625 4 Discussion

### 626 4.1 The importance of liquid water path constraint

627 LWP is a critical parameter governing cloud radiative properties (Murray-Watson et al., 2022). The  
628 quantification of albedo effects strongly depends on the spatial scale and the LWP. Neglecting LWP  
629 constraints in ~~aerosol-cloud-interaction~~ studies can weaken microphysical signals, leading to  
630 underestimation of radiative forcing (McComiskey et al., 2012). To address this, we first systematically  
631 investigated the dynamic relationship between CER and LWP before analyzing CER sensitivity to AOD.  
632 The results demonstrate pronounced CER sensitivity to LWP variations, which can be categorized into  
633 three distinct regimes (Figure 4):

634 In the first LWP regime, CER increases rapidly with LWP, i.e. the evolution of CER is predominantly  
635 driven by changes in LWP. This dominance may lead to overestimation of the influence of the AOD on  
636 CER (Liu et al., 2021).

637 In the second LWP regime, CER decreases with increasing LWP. In this regime, the regulatory effect of  
638 LWP on CER weakens significantly, and CER variations become increasingly governed by aerosol-  
639 related processes, indicating the growing dominance of aerosol indirect effects.

640 The third regime contains an insufficient number of CER observations to yield statistically significant  
641 results, which excludes the analysis of the sensitivity of CER to AOD.

642 Comparative analysis of scale-conditioned  $S_{CER}$  across LWP regimes in periods 1 and 2 revealed  
643 markedly enhanced sensitivity of  $S_{CER}$  to AOD in the second LWP regime. ~~There is a trade-off exists~~

644 ~~between AOD and LWP when the amount of under conditions of insufficient water vapor, is insufficient~~  
645 ~~and. This trade-off leads to smaller CER values. CER becomes smaller.~~ As suggested by Costantino et

646 al. (2013), the LWP response to aerosol invigoration is influenced by two competing mechanisms: a  
647 drying effect caused by enhanced entrainment of dry air at cloud top (dominant in optically thin clouds)  
648 and a moistening effect from precipitation suppression (dominant in optically thick clouds). ~~For larger~~

649 ~~LWP, the supply of cloud water is sufficient, and t. The increase in aerosol number concentrations~~  
650 ~~significantly affects the distribution of cloud droplet number concentrations and sizes. This further~~

651 ~~enhances~~ the sensitivity of CER to AOD. For small aerosol concentrations, the values of  $|S_{CER}|$  (Figure

652 5b, 7b) decreased overall with expanding buffer size within the same study area. For fixed buffer size,  
653  $|S_{CER}|$  decreased as the study area increased, and the ranges of  $|S_{CER}|$  values across different study areas  
654 showed a convergent pattern. These values typically remained small and (close to zero). During the  
655 high AOD period (2008–2014), anthropogenic emissions and dust transport provided abundant CCN,  
656 laying the material foundation for strong aerosol-cloud interactions. This enhanced the  
657 synergistic effect of “sufficient liquid water + abundant CCN” in the second LWP regime. This  
658 synergistic effect amplified the difference in  $S_{CER}$  between the two LWP regimes. In the period of  
659 decreasing AOD (2015–2022), CCN concentration following the implementation of  
660 clean air policies (de Leeuw et al., 2021; 2023), CCN concentration decreased (Wang et al., 2023). This  
661 reduction weakened the direct impact of aerosols on CER. However, the LWP-driven microphysical  
662 differences persisted, so  $S_{CER}$  in the second regime remained significantly smaller than that in the  
663 first regime, albeit with a smaller difference. Additionally, the complexity of aerosol types during the  
664 high AOD period (e.g., mixing of anthropogenic pollutants and natural dust) may have adjusted the value  
665 of  $S_{CER}$ . However, it did not alter the dominant role of LWP. This aligns with the theory that “aerosol  
666 indirect effects are jointly regulated by concentration and type” (Liu et al., 2017).

667 The larger  $S_{CER}$  observed at larger spatial scales (Figures 5 and 7) may be attributed to meteorological  
668 confounding effects. In addition, clouds with larger LWP are usually associated with strong updrafts  
669 (such as convective clouds), and stronger turbulence and vertical transport will bring more aerosols into  
670 the clouds, increasing CCN concentration and a decrease in particle size, making them more sensitive to  
671 changes in AOD (Jones et al., 2009; Han et al., 2022; Fan et al., 2025). Therefore, this phenomenon is  
672 the result of the combined action of cloud microphysical processes (CCN activation, cloud droplet  
673 competition growth) and dynamic processes (updrafts, turbulent mixing). If the characteristics of aerosols  
674 (such as composition) change in the second LWP regime, this sensitivity may be further amplified.  
675 Consequently, the LWP-stratified  $S_{CER}$  quantification framework enables precise characterization of  
676 scale-dependent aerosol-cloud interactions, providing robust physical insights for climate effect  
677 assessments and effectively reducing uncertainties in future climate projections.

678 The central hypothesis of this study—that LWP is relatively consistent between the two periods (2008–  
679 2014 and 2015–2022), supporting valid comparisons of the spatial sensitivity of AOD-CER  
680 relationships—is well-supported by the following analysis. The differences in the mean, median, 25th,

681 and 50th percentiles of LWP between the two periods are all less than 5%, indicating a stable overall  
682 water vapor supply level. The spatial patterns of high-LWP regions (e.g., southeastern areas) and low-  
683 LWP regions (e.g., the mountainous areas in northern Shanxi) remained stable across the two periods  
684 (see Appendix B1), demonstrating **that** LWP spatial distribution characteristics are highly consistent. The  
685 sample proportions of LWP in the rapid growth regime are 59.30% (period 1: 0–55 g/m<sup>2</sup>) and 55.36%  
686 (period 2: 0–50 g/m<sup>2</sup>), while those in the decreasing regime are 29.64% (period 1: 55–135 g/m<sup>2</sup>) and  
687 24.59% (period 2: 50–100 g/m<sup>2</sup>), suggesting that there is no systematic temporal shift in the LWP  
688 distribution. Meanwhile, short-term fluctuations are smoothed by multi-year averaging and large-sample  
689 statistics, resulting in a weak indirect impact of aerosols on LWP (LWP only increased by 5.6%, much  
690 smaller than the 24% decrease in AOD). Additionally, LWP-stratified analysis (**i.e., binning LWP into**  
691 **5 g m<sup>-2</sup> intervals**) further isolates interference. The validation of the core hypothesis provides a reliable  
692 premise for accurately quantifying the impact of aerosol concentration changes on the sensitivity of cloud  
693 parameters and their spatial scale dependence.

#### 694 **4.2 Scale dependence of cloud parameters sensitivities to aerosol variations**

695 Extensive studies have demonstrated a significant spatial scale dependence of aerosol indirect effects  
696 (McComiskey et al., 2012; Possner et al., 2016; Glotfelty et al., 2020; Ekman et al., 2023). Failure to  
697 explicitly define the scale-dependent behavior of aerosol indirect effects may introduce systematic biases  
698 and inconsistencies in subsequent process analyses. Based on satellite observations, this study confirms  
699 statistically significant negative correlations between CER and AOD, as well as positive correlations  
700 between N<sub>d</sub> and AOD during periods with different aerosol concentrations, aligning with classical  
701 **aerosol-cloud-interaction-aci** theory (Quaas et al., 2009). Analysis of scale-conditioned S<sub>CER</sub> and S<sub>N<sub>d</sub></sub>  
702 reveals that for fixed buffer size, an increase in the size of the study area leads to a systematic reduction  
703 in S<sub>CER</sub> (less negative) and S<sub>N<sub>d</sub></sub>, corroborating the nonlinear attenuation of aerosol signals with spatial  
704 domain expansion (Quaas et al., 2009). The results from this study suggest that AOD-cloud property  
705 correlations in large study areas are susceptible to meteorological confounding effects (Quaas et al., 2010;  
706 Boucher and Quaas, 2012; Gryspeerdt et al., 2014; Liu et al., 2024). Theoretically, aerosol regulation of  
707 cloud microphysics is strongly local: smaller domains (e.g., 4°×4°) feature homogeneous meteorological  
708 conditions (humidity, updrafts), preserving undiluted **aerosol-cloud-interaction-aci** signals and yielding

709 larger  $|S_{CER}|$  (pronounced Twomey effect). In contrast, expanded domains (e.g.,  $10^\circ \times 10^\circ$ ) encompass  
710 heterogeneous meteorological conditions (circulation differences, boundary layer variability) that  
711 independently modulate cloud droplet growth. For example, strong updrafts enhance liquid water supply,  
712 offsetting aerosol-induced radius reduction (Altartatz et al., 2014), weakening aerosol-CER correlations  
713 and reducing  $|S_{CER}|$ . Consistent with Grandey & Stier (2010), large-scale domains introduce “dilution  
714 bias” via non-target meteorological variability. This scale-dependent confounding mechanism elucidates  
715 uncertainties in aerosol indirect effect assessments at regional scales.

716 Multi-scale spatial analysis identifies different optimal buffer sizes for  $S_{CER}$  and  $S_{Nd}$  in different periods.  
717 These findings align closely with satellite-based aerosol indirect effect studies (Wang et al., 2015; Liu et  
718 al., 2017), providing critical scale benchmarks for satellite product validation. Wang et al. (2015) reported  
719 an inverse “Twomey” effect between aerosols and CER in eastern China by analyzing aerosol and CER  
720 within a 50 km buffer zone around CALIOP samples. Similarly, Liu et al. (2017) systematically examined  
721 the response mechanisms of warm cloud macro- and microphysical parameters to increasing AOD in the  
722 Yangtze River Delta region, also using CALIOP samples within a 50 km buffer zone. The present study  
723 further shows that, as aerosol concentrations decrease,  $S_{CER}$  values across different study areas with the  
724 same buffer size exhibit convergence characteristics, with generally smaller  $S_{CER}$  (closer to zero). This  
725 indicates a significant weakening of aerosol-cloud interaction intensity and reduced spatial extent  
726 dependency in low aerosol loading conditions. This phenomenon is consistent with the simulated  
727 behavior of aerosol-limited cloud regimes, where aerosol-cloud interactions are quantitatively  
728 modulated by moisture availability and lose their sensitivity to large-scale dynamical stability, leading to  
729 a weaker and more homogeneous effect (Zhao et al., 2025).

730 By systematically quantifying the scale-response characteristics of aerosol indirect effects, this work not  
731 only elucidates the dynamic scale behavior of aerosol-cloud interactions but, but also, more critically,  
732 establishes criteria for determining optimal buffer size in regional aerosol indirect effect studies. These  
733 results provide quantitative observational constraints for refining scale-dependent parameterization  
734 modules in climate models, particularly for representing the modulation of ACI by spatial scale and LWP,  
735 thereby improving model predictive reliability. Such advancements provide actionable insights for  
736 refining parameterization schemes in climate models, thereby enhancing their predictive reliability.

### 737 4.3 Contrasting sensitivity patterns of cloud parameters in response to AOD

738 A comprehensive comparison of the sensitivity  $S_{CER}$  and  $S_{Nd}$  reveals that the responses of CER and  $N_d$  to  
739 AOD exhibit distinct yet inherently interconnected characteristics. These characteristics are jointly  
740 modulated by spatial scale and LWP regimes (Figs. 5, 7, 8; Appendices A1–A2), which profoundly reflect  
741 the core microphysical mechanisms of [aerosol–cloud interactions](#). Details are elaborated as follows:

#### 742 4.3.1 Core differences in response modes between $S_{CER}$ and $N_d$ to AOD

743  $S_{CER}$  is consistently negative across both periods and all LWP regimes ( $-0.33 < S_{CER} < 0$ ) (Figs. 5, 7;  
744 Appendix A1), indicating that an increase in AOD leads to a decrease in CER. This aligns with the core  
745 principle of the Twomey effect (Twomey, 1977; Feingold et al., 2001). The values of  $|S_{CER}|$  are larger in  
746 the second LWP regime than in the first regime, reflecting stronger aerosol modulation of cloud  
747 microphysical properties when liquid water is abundant (McComiskey & Feingold, 2012). In contrast,  
748  $S_{Nd}$  maintains a significant positive correlation with AOD across all scenarios ( $0 < S_{Nd} < 1$ ) (Fig. 8;  
749 Appendix A2), confirming that higher AOD directly promotes CCN activation and thereby increases  
750 cloud droplet number concentration (Andreae, 2009). [S<sub>Nd</sub> is larger in small-scale study areas \(e.g., 4°×4°\)](#)  
751 [and small buffer zones, with a maximum value of 0.45 in the first period, indicating greater sensitivity](#)  
752 [of cloud droplet number to aerosol loading at fine spatial scales.](#)

#### 753 4.3.2 Synergistic modulation of AOD and spatial scale

754 Using the LWP interval corresponding to  $S_{Nd}$  ( $0 < LWP \leq 200$  g/m<sup>2</sup>) as a benchmark, comparisons  
755 between the two periods (incorporating average values of  $S_{CER}$  across two LWP regimes) reveal distinct  
756 characteristics:

757 For the small-scale study area (4°×4°): In period 1, the average  $|S_{CER}|$  across two LWP regimes is 0.271  
758 (0.2232 for the 0–55 g/m<sup>2</sup> LWP regime, 0.3189 for the 55–135 g/m<sup>2</sup> LWP regime) and  $S_{Nd}=0.4496$ , both  
759 significantly higher than those in period 2 (average  $|S_{CER}|=0.154$ , with 0.0863 for [the](#) 0–50 g/m<sup>2</sup> LWP  
760 regime and 0.2212 for [the](#) 50–100 g/m<sup>2</sup> LWP regime;  $S_{Nd}=0.2903$ ). The negative correlation between  
761 AOD and CER is more significant in period 1, as sufficient CCN in small-scale areas amplifies both  
762 cloud droplet number increase and size reduction, enhancing the Twomey effect.

763 For the medium-to-large scale study areas ( $6^\circ \times 6^\circ$ ,  $8^\circ \times 8^\circ$ ,  $10^\circ \times 10^\circ$ ): In period 1, the average  $|S_{\text{CER}}|$  across  
764 the two LWP regimes is 0.1683 (0.1305 for 0–55 g/m<sup>2</sup>, 0.2061 for 55–135 g/m<sup>2</sup>), 0.13065 (0.1026 for 0–  
765 55 g/m<sup>2</sup>, 0.1587 for 55–135 g/m<sup>2</sup>), and 0.1067 (0.0858 for 0–55 g/m<sup>2</sup>, 0.0885 for 55–135 g/m<sup>2</sup>),  
766 respectively, all higher than the corresponding values in period 2 (0.1516, 0.1246, 0.0985). However,  $S_{\text{Nd}}$   
767 in period 1 (0.2430, 0.2050, 0.1430) is lower than that in period 2 (0.2960, 0.2680, 0.1740), with no  
768 significant difference in the negative correlation between AOD and CER between the two periods.  
769 This characteristic indicates that meteorological confounding effects are enhanced at larger scales,  
770 weakening the regulation of  $S_{\text{Nd}}$  by aerosols, while at small scales the aci is directly driven by AOD levels.

### 771 4.3.3 Implications for aerosol indirect effects

772 The differences and interconnections between  $S_{\text{CER}}$  and  $S_{\text{Nd}}$  highlight that aerosol indirect effects are  
773 dominated by coupled microphysical processes: Aerosol induced increases in CCN first enhance  $N_d$   
774 through positive  $S_{\text{Nd}}$ , and then reduce CER through negative  $S_{\text{CER}}$  under constant LWP conditions. The  
775 scale dependent attenuation of both sensitivities and their modulation by LWP indicate that quantifying  
776 aerosol indirect effects requires full consideration of spatial scales and the key role of liquid water,  
777 providing observational basis for optimizing climate model parameterization schemes.

### 778 4.4 Limitations and future perspectives

779 This study has three significant limitations. Firstly, similar to most previous studies (Wang et al., 2015;  
780 Liu et al., 2021), this study only utilized MODIS data with a resolution of 10 km to explore scale effects,  
781 ignoring finer or coarser resolution data. Therefore, using a 10 km buffer size as the minimum  
782 observation unit, this limitation makes the indirect effects of aerosols on smaller scales still unknown,  
783 which may lead to inaccurate evaluation of aerosol indirect effects. Therefore, future research can  
784 improve the sensitivity of aerosol indirect effects to scale changes by using observation data with higher  
785 accuracy or model simulations. Secondly, the current research focuses on the influence of buffer size and  
786 study areas, the potential impact of spatial aggregation methods (especially zoning directionality) on the  
787 quantitative results of aerosol indirect effects has not been systematically evaluated. Future research  
788 should further investigate the sensitivity of aerosol indirect effects to zoning direction. Moreover, the  
789 current study employs a uniform buffer size for both aerosol and cloud parameters, failing to account for

790 potential interaction effects arising from discrepancies of buffer size between them. Therefore, clarifying  
791 scale dependence will avoid directly extrapolating local observation results to a larger study area when  
792 downscaling climate models or formulating regional environmental policies.

## 793 **5 Conclusions**

794 Based on MODIS and CALIOP satellite observations of aerosol and cloud parameters over land in eastern  
795 China, a comparative analysis was conducted of the sensitivity of cloud microphysical parameters (CER  
796 and  $N_d$ ) to variations in AOD during two characteristic periods: 2008–2014 (period 1, high AOD) and  
797 2015–2022 (period 2, decreasing AOD). Through systematic analysis of the relationship between CER  
798 and LWP and their response mechanisms to AOD across these two periods, the following key conclusions  
799 were drawn:

800 Firstly, CER exhibited three distinct regimes with varying LWP. During the rapid growth regime (LWP  
801  $< 55/50 \text{ g/m}^2$ ), CER showed significant negative sensitivity to AOD ( $S_{\text{CER}}$ ), consistent with the Twomey  
802 effect; during the decreasing regime (LWP = 55-135/50-100  $\text{g/m}^2$ ),  $S_{\text{CER}}$  remained negative but with  
803 enhanced sensitivity; and during the slow growth regime (LWP  $> 135/100 \text{ g/m}^2$ ), the rate of CER change  
804 significantly decreased. These findings confirmed that LWP is a crucial, regulatory factor influencing the  
805 CER response to AOD.

806 Secondly, scale dependence analysis led to the conclusion that characteristics in **aerosol-cloud**  
807 **interactionaci** are significantly scale-dependent, with systematic variations of both  $S_{\text{CER}}$  and  $S_{N_d}$  with  
808 changes in buffer size and study area. The results of the study show that  $S_{\text{CER}}$  systematically increased as  
809 buffer size increased and became negligible for buffer sizes larger than 150-200 km, while the optimal  
810 buffer sizes varied substantially with the size of the study area in the range from  $6^\circ \times 6^\circ$  to  $10^\circ \times 10^\circ$ :  
811 increased as study area increased during period 2, but decreased in period 1 for regime 2. Particularly  
812 noteworthy is the enhanced consistency of  $S_{\text{CER}}$  across different study areas and the significant increase  
813 in  $S_{\text{CER}}$  during period 2, reflecting weaker **aerosol-cloud interactionsaci** due to declining regional aerosol  
814 concentrations.

815 Finally, the sensitivity of  $N_d$  to AOD ( $S_{N_d}$ ) exhibited distinct characteristics compared to  $S_{\text{CER}}$ :  $S_{N_d}$  showed  
816 a significant positive correlation ( $p < 0.01$ ) and demonstrated nonlinear attenuation with increasing buffer  
817 size and study area. The optimal buffer size for  $S_{N_d}$  was smaller during period 2 than during period 1 and

818 increased with the study area size, being substantially larger for study areas of  $8^\circ \times 8^\circ$  and  $10^\circ \times 10^\circ$  than  
 819 for study areas of  $4^\circ \times 4^\circ$  and  $6^\circ \times 6^\circ$  areas.

820 These observed patterns correspond to the fundamental microphysical pathway of aci, whereby increased  
 821 aerosol loading enhances  $N_d$  and reduces CER under constant LWP conditions. The results emphasize  
 822 that accurate quantification of ACI must explicitly consider both the phase-dependent characteristics of  
 823 LWP and spatial scale effects when assessing aerosol indirect effects.

824 ~~These findings not only deepen our understanding of aerosol indirect effects but also provide an~~  
 825 ~~important observational basis for improving aerosol cloud parameterization schemes in climate models.~~

826 These findings deepen our understanding of aerosol indirect effects and provide quantitative  
 827 observational constraints for improving aerosol cloud parameterization in climate models. Our results  
 828 highlight that ACI parameterization should explicitly incorporate LWP regime-dependent behavior and  
 829 spatial scale-dependent interaction strengths to improve realistic representation. The results emphasize  
 830 that both the phased characteristics of LWP and spatial scale effects must be considered when assessing  
 831 aerosol indirect effects.

## 832 Appendix

833 **A1. Estimates of  $S_{CER}$ , computed using Eq. (1), and correlation coefficients R between CER and AOD,**  
 834 **stratified by LWP, and optimal buffer size (see text), for study areas varying from  $4^\circ \times 4^\circ$  to  $10^\circ \times 10^\circ$ , during**  
 835 **the periods 2008-2014 and 2015-2022. Statistically significant data points are indicated with \* (p value < 0.01).**

Years	LWP ( $g/m^2$ )	Study area	Optimal scale (km)	$S_{CER}$	R
2008-2014	0-55	$10^\circ \times 10^\circ$	30	-0.0858	0.8828*
		$8^\circ \times 8^\circ$	40	-0.1026	0.9220*
		$6^\circ \times 6^\circ$	100	-0.1305	0.8939*
	55-135	$4^\circ \times 4^\circ$	50	-0.2232	0.8459*
		$10^\circ \times 10^\circ$	40	-0.1275	0.8377*
		$8^\circ \times 8^\circ$	60	-0.1587	0.8978*
2015-2022	0-50	$6^\circ \times 6^\circ$	30	-0.2061	0.9245*
		$4^\circ \times 4^\circ$	50	-0.3189	0.9096*
		$10^\circ \times 10^\circ$	80	-0.0885	0.9082*
	50-100	$8^\circ \times 8^\circ$	40	-0.1138	0.8886*
		$6^\circ \times 6^\circ$	20	-0.1517	0.7618*
		$4^\circ \times 4^\circ$	50	-0.0863	0.6403*
		$10^\circ \times 10^\circ$	100	-0.1084	0.8717*
		$8^\circ \times 8^\circ$	90	-0.1354	0.8910*
		$6^\circ \times 6^\circ$	60	-0.1514	0.8384*
		$4^\circ \times 4^\circ$	60	-0.2212	0.8318*

836  
837  
838  
839  
840  
841  
842  
843  
844  
845  
846  
847

**A2. Estimates of  $S_{Nd}$ , computed using Eq. (2), and correlation coefficients  $R$  between  $N_d$  and AOD, stratified by optimal buffer size (see text) for study areas varying from  $4^\circ \times 4^\circ$  to  $10^\circ \times 10^\circ$ , during the periods 2008-2014 and 2015-2022. Statistically significant data points are indicated with \* ( $p$  value < 0.01).**

Years	Study area	Optimal scale (km)	$S_{Nd}$	$R$
2008-2014	$10^\circ \times 10^\circ$	70	0.1434	-0.8507*
	$8^\circ \times 8^\circ$	80	0.2045	-0.8646*
	$6^\circ \times 6^\circ$	30	0.2430	-0.8741*
	$4^\circ \times 4^\circ$	40	0.4496	-0.8523*
2015-2022	$10^\circ \times 10^\circ$	60	0.1742	-0.8788*
	$8^\circ \times 8^\circ$	60	0.2682	-0.8638*
	$6^\circ \times 6^\circ$	20	0.2964	-0.6900*
	$4^\circ \times 4^\circ$	30	0.2903	-0.7478*

848  
849  
850

**A3. Sample sizes of cloud droplet effective radius (CER) and aerosol optical depth (AOD) across different buffer sizes, study areas (LWP regime 1, 2008–2014).**

Buffer sizes	Sample sizes of CER in LWP regime 1				Sample sizes of AOD in LWP regime 1			
	$10^\circ \times 10^\circ$	$8^\circ \times 8^\circ$	$6^\circ \times 6^\circ$	$4^\circ \times 4^\circ$	$10^\circ \times 10^\circ$	$8^\circ \times 8^\circ$	$6^\circ \times 6^\circ$	$4^\circ \times 4^\circ$
10	25054	16133	8551	3879	47846	32406	18711	8808
20	41667	26507	14077	6376	64878	42949	24462	11377
30	54960	34885	18421	8346	76569	50055	28274	13047
40	66170	42147	22136	9966	86291	56006	31523	14482
50	76207	48769	25738	11593	94726	61227	34272	15664
60	85194	54539	28946	12979	102262	65860	36741	16695
70	93413	59681	31788	14192	108792	69756	38749	17519
80	100728	64370	34330	15317	114357	73103	40498	18246
90	107291	68535	36552	16270	119187	76077	42016	18893
100	113457	72525	38761	17155	123607	78839	43496	19469
120	124793	79882	42945	18964	131449	83807	46217	20534
140	134597	86324	46525	20462	138140	88001	48518	21557
150	138760	89086	48145	21141	141012	89985	49570	21991
160	142693	91808	49602	21734	143725	91767	50570	22436
180	150015	96789	52326	22860	148480	94870	52385	23155
200	156655	101246	54894	23983	153084	97946	53963	23921
250	169423	109475	59449	26008	162530	104346	56987	25388
300	178015	115051	62656	27442	170117	109006	59332	26453

851

852

**A4. Sample sizes of cloud droplet effective radius (CER) and aerosol optical depth (AOD) across different buffer sizes, study areas (LWP regime 2, 2008–2014).**

853

Buffer sizes	Sample sizes of CER in LWP regime 2				Sample sizes of AOD in LWP regime 2			
	10°×10°	8°×8°	6°×6°	4°×4°	10°×10°	8°×8°	6°×6°	4°×4°
10	22338	14357	7737	3715	47846	32406	18711	8808
20	35406	22471	11964	5697	64878	42949	24462	11377
30	45473	28805	15162	7187	76569	50055	28274	13047
40	54074	34078	17839	8368	86291	56006	31523	14482
50	61579	38732	20290	9444	94726	61227	34272	15664
60	68173	43017	22553	10424	102262	65860	36741	16695
70	74272	46909	24584	11230	108792	69756	38749	17519
80	79999	50507	26412	11950	114357	73103	40498	18246
90	85339	53806	28177	12654	119187	76077	42016	18893
100	90440	56944	29812	13329	123607	78839	43496	19469
120	99758	62598	32673	14486	131449	83807	46217	20534
140	108723	68273	35600	15795	138140	88001	48518	21557
150	112740	70969	36864	16426	141012	89985	49570	21991
160	116558	73463	38046	16974	143725	91767	50570	22436
180	123653	78031	40203	17917	148480	94870	52385	23155
200	129864	81813	42186	18674	153084	97946	53963	23921
250	142429	89112	46079	20120	162530	104346	56987	25388
300	152460	95213	49452	21369	170117	109006	59332	26453

854

855

**A5. Sample sizes of cloud droplet effective radius (CER) and aerosol optical depth (AOD) across different buffer sizes, study areas (LWP regime 1, 2015–2022).**

856

Buffer sizes	Sample sizes of CER in LWP regime 1				Sample sizes of AOD in LWP regime 1			
	10°×10°	8°×8°	6°×6°	4°×4°	10°×10°	8°×8°	6°×6°	4°×4°
10	25054	16133	8551	3879	47846	32406	18711	8808
20	41667	26507	14077	6376	64878	42949	24462	11377
30	54960	34885	18421	8346	76569	50055	28274	13047
40	66170	42147	22136	9966	86291	56006	31523	14482
50	76207	48769	25738	11593	94726	61227	34272	15664
60	85194	54539	28946	12979	102262	65860	36741	16695
70	93413	59681	31788	14192	108792	69756	38749	17519
80	100728	64370	34330	15317	114357	73103	40498	18246
90	107291	68535	36552	16270	119187	76077	42016	18893
100	113457	72525	38761	17155	123607	78839	43496	19469
120	124793	79882	42945	18964	131449	83807	46217	20534
140	134597	86324	46525	20462	138140	88001	48518	21557
150	138760	89086	48145	21141	141012	89985	49570	21991
160	142693	91808	49602	21734	143725	91767	50570	22436
180	150015	96789	52326	22860	148480	94870	52385	23155
200	156655	101246	54894	23983	153084	97946	53963	23921

250 169423 109475 59449 26008 162530 104346 56987 25388

857

858 **A6. Sample sizes of cloud droplet effective radius (CER) and aerosol optical depth (AOD) across different**  
 859 **buffer size, study areas (LWP regime 2, 2015–2022).**

Buffer sizes	Sample sizes of CER in LWP regime 2				Sample sizes of AOD in LWP regime 2			
	10°×10°	8°×8°	6°×6°	4°×4°	10°×10°	8°×8°	6°×6°	4°×4°
10	6548	6548	5449	2803	12892	12892	12892	5961
20	24886	16258	8833	4421	46067	30536	17623	8079
30	32260	20786	11214	5490	55767	36685	20780	9408
40	38784	24739	13284	6440	63457	41493	23310	10474
50	44831	28399	15176	7183	70030	45443	25423	11419
60	50181	31609	16909	7816	75667	48900	27138	12122
70	54865	34476	18456	8415	80872	51807	28559	12723
80	58946	37042	19776	8901	85308	54361	29846	13245
90	62835	39437	21006	9359	89202	56659	31024	13706
100	66623	41757	22165	9796	92939	58931	32143	14126
120	73427	46010	24248	10605	99298	62674	34081	14927
140	79486	49854	26210	11312	104540	65994	36013	15617
150	82336	51650	26988	11633	107089	67545	36876	15939
160	85055	53440	27893	11942	109626	69104	37718	16261
180	89669	56388	29401	12520	114187	72088	39380	16889
200	93898	58986	30700	13034	117969	74508	40596	17401
250	102933	64417	33649	14040	125590	79489	43005	18271
300	109964	68913	35755	14701	132000	83404	45012	18913

860

861 **A7. Sample sizes of cloud droplet number concentration (Na) and aerosol optical depth (AOD) across different**  
 862 **buffer sizes and study areas during 2008-2014.**

Buffer sizes	Sample sizes of Na				Sample sizes of AOD			
	10°×10°	8°×8°	6°×6°	4°×4°	10°×10°	8°×8°	6°×6°	4°×4°
10	47846	32406	18711	8808	50686	32611	17320	8053
20	64878	42949	24462	11377	70102	45066	23944	11084
30	76569	50055	28274	13047	84442	54334	28822	13435
40	86291	56006	31523	14482	96186	62056	32857	15309
50	94726	61227	34272	15664	106166	68620	36473	16906
60	102262	65860	36741	16695	114950	74328	39638	18292
70	108792	69756	38749	17519	122840	79508	42510	19478
80	114357	73103	40498	18246	129763	84048	45038	20599
90	119187	76077	42016	18893	135810	87931	47225	21548
100	123607	78839	43496	19469	141407	91543	49256	22436
120	131449	83807	46217	20534	151353	98040	53031	24145
140	138140	88001	48518	21557	159758	103516	56167	25517
150	141012	89985	49570	21991	163180	105820	57561	26100
160	143725	91767	50570	22436	166373	108000	58769	26661

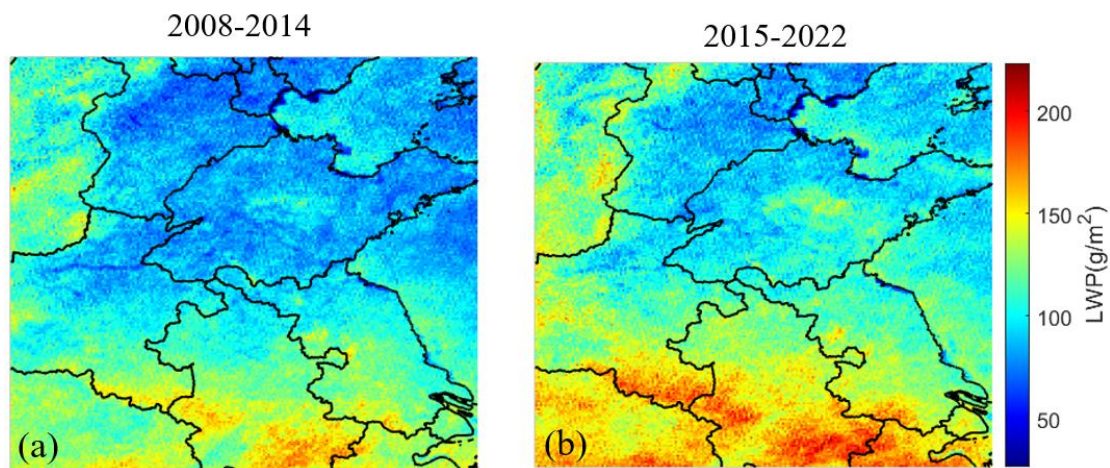
180	148480	94870	52385	23155	172007	111773	60981	27665
200	153084	97946	53963	23921	176658	114922	62862	28696
250	162530	104346	56987	25388	185393	120627	66331	30409
300	170117	109006	59332	26453	191138	124592	68823	31481

863

864 **A8. Sample sizes of cloud droplet number concentration ( $N_a$ ) and aerosol optical depth (AOD) across different**  
865 **buffer sizes and study areas during 2015-2022.**

Buffer sizes	Sample sizes of $N_a$				Sample sizes of AOD			
	$10^\circ \times 10^\circ$	$8^\circ \times 8^\circ$	$6^\circ \times 6^\circ$	$4^\circ \times 4^\circ$	$10^\circ \times 10^\circ$	$8^\circ \times 8^\circ$	$6^\circ \times 6^\circ$	$4^\circ \times 4^\circ$
10	37182	23994	13048	6149	31621	21503	12892	5961
20	51313	32990	17755	8252	46067	30536	17623	8079
30	61921	39800	21327	9788	55767	36685	20780	9408
40	70663	45351	24213	11063	63457	41493	23310	10474
50	78059	50080	26808	12118	70030	45443	25423	11419
60	84354	53975	28967	13015	75667	48900	27138	12122
70	89675	57448	30881	13832	80872	51807	28559	12723
80	94620	60671	32636	14556	85308	54361	29846	13245
90	99042	63497	34138	15155	89202	56659	31024	13706
100	102936	65993	35444	15703	92939	58931	32143	14126
120	110590	70884	38002	16787	99298	62674	34081	14927
140	116487	74472	40007	17549	104540	65994	36013	15617
150	119140	76230	41049	17958	107089	67545	36876	15939
160	121506	77846	41958	18265	109626	69104	37718	16261
180	125788	80845	43582	18935	114187	72088	39380	16889
200	129613	83370	44887	19538	117969	74508	40596	17401
250	136752	87967	47756	20784	125590	79489	43005	18271
300	141896	91273	49807	21431	132000	83404	45012	18913

866



867

868 **B1. Spatial distributions of LWP averaged over the years 2008-2014 (a) and 2015-2022 (b) over the study area.**

869 **The lines are provincial borders and the names of provinces mentioned in the text are indicated in Fig. 3(f).**

870 **Data availability**

871 All data used in this study are publicly available. The satellite data from the MODIS instrument used in  
872 this study were obtained from <https://ladsweb.nascom.nasa.gov/search/> (last access: 02 July 2025). The  
873 satellite data from CALIOP were obtained from <https://subset.larc.nasa.gov/calipso/login.php> (last  
874 access: 02 July 2025).

875 **Author contributions**

876 YL, LT and GL designed the research. YL and LT led the analyses. YL and GL wrote the manuscript  
877 with major input from JH, and further input from all other authors. All authors contributed to interpreting  
878 the results and to the finalization and revision of the manuscript.

879 **Competing interests**

880 The authors declare that they have no conflict of interest.

881 **Acknowledgements**

882 The authors greatly appreciate NASA CloudSat Data Processing Center that provided the data used in  
883 this study. This work was supported by the National Natural Science Foundation of China (Grant No.  
884 42001290), the National Natural Science Foundation of China (Grant No. 42271299), the Natural Science  
885 Foundation Project of Xiamen (Grant No. 3502Z202472037) and the Chinese Academy of Sciences  
886 President's International Fellowship Initiative, Grant No. 2025PVA0014\_Y1.

887 **References**

888 Albrecht, B. A.: Aerosols, cloud microphysics, and fractional cloudiness, *Science*, 245, 1227-1230, 1989.  
889 Bellouin, N., Quaas, J., Gryspeerdt, E., Kinne, S., Stier, P., Watson-Parris, D., et al.: Bounding global  
890 aerosol radiative forcing of climate change. *Reviews of Geophysics*, 58, e2019RG000660.  
891 <https://doi.org/10.1029/2019RG000660>, 2020.  
892 Altaratz, O., Koren, I., Remer, L.A., Hirsch, E.: Review: Cloud invigoration by aerosols—Coupling  
893 between microphysics and dynamics. *Atmospheric Research*, 140-141, 38-60, 2014.

894 Andreae, M. O.: Correlation between cloud condensation nuclei concentration and aerosol optical  
895 thickness in remote and polluted regions, *Atmos. Chem. Phys.*, 9, 543-556, [https://doi.org/10.5194/acp-](https://doi.org/10.5194/acp-9-543-2009)  
896 9-543-2009, 2009.

897 Baum, B. A., et al.: MODIS cloud-top property refinement for Collection 6, *J. Appl. Meteorol. Climatol.*,  
898 51(6), 1145-1163, 2012.

899 Bender, F.A.M., Frey, L., McCoy, D.T., Grosvenor, D.P., Mohrmann, J.K.: Assessment of aerosol–  
900 cloud–radiation correlations in satellite observations, climate models and reanalysis. *Climate Dynamics*,  
901 52, 4371-4392, 2019.

902 Boucher, O., Quaas, J.: Water vapour affects both rain and aerosol optical depth. *Nature Geoscience*, 6(1),  
903 4-5. <https://doi.org/10.1038/ngeo1692>, 2012.

904 Bréon, F. M., Tanré, D., Generoso, S.: Aerosol effect on cloud droplet size monitored from satellite,  
905 *Science*, 295(5556):834-8. doi: 10.1126/science.1066434, 2002.

906 Bulgin, C. E., Palmer, P.I., Thomas, G.E., Arnold, C.P.G., Campmany, E., Carboni, E., Grainger, R. G.,  
907 Poulsen, C., Siddans, R., Lawrence, B.N.: Regional and seasonal variations of the Twomey indirect effect  
908 as observed by the ATSR-2 satellite instrument, *Geophysical Research Letters*, 35, 2, 2008.

909 Cai, H., Yang, Y., Chen, Q.: Distribution Characteristics of Cloud Types and Cloud Phases over China  
910 and Their Relationship with Cloud Temperature, *Remote Sensing*, 14(21), 2022.  
911 <https://doi.org/10.3390/rs14215601>

912 Chen, G., W.-C.Wang, and J.-P. Chen, 2015: Aerosol–stratocumulus–radiation interactions over  
913 southeast Pacific. *J. Atmos. Sci.*, 72, 2612–2621, <https://doi.org/10.1175/JAS-D-14-0319.1>.

914 Chen, Y.-C., Christensen, M. W., Stephens, G. L., and Seinfeld, J. H.: Satellite-based estimate of global  
915 aerosol-cloud radiative forcing by marine warm clouds, *Nat. Geosci.*, 7, 643–646,  
916 <https://doi.org/10.1038/ngeo2214>, 2014.

917 Christensen, M. W., Chen, Y.-C., and Stephens, G. L.: Aerosol indirect effect dictated by liquid clouds,  
918 *J. Geophys. Res.*, 121, 14636-14650, <https://doi.org/10.1002/2016JD025245>, 2016.

919 Costantino, L. and Bréon, F. M.: Analysis of aerosol-cloud interaction from multi-sensor satellite  
920 observations. *Geophys. Res. Lett.*, 37, L11801, doi:10.1029/2009GL041828, 2010.

921 Costantino, L. and Bréon, F. M.: Aerosol indirect effect on warm clouds over South-East Atlantic, from  
922 co-located MODIS and CALIPSO observations, *Atmos. Chem. Phys.*, 13: 69-88, 2013.

923 Dagan, G., Yeheskel, N., Williams, A. I. L.: Radiative forcing from aerosol–cloud interactions enhanced  
924 by large-scale circulation adjustments, *Nature geoscience*, 16, 1092-1098, 2023.

925 de Leeuw, G., R. van der A, J. Bai, Y. Xue, C. Varotsos, Z. Li, C. Fan, X. Chen, I. Christodoulakis, J.  
926 Ding, X. Hou, G. Kouremadas, D. Li, J. Wang, M. Zara, K. Zhang, Y. Zhang.: Air Quality over China.  
927 *Remote Sens.* 2021, 13, 3542. [https://doi.org/ 10.3390/rs13173542](https://doi.org/10.3390/rs13173542), 2021.

928 de Leeuw, G., Fan, C, Li, Z., Dong, J., Li, Y., Ou, Y., and Zhu, S. (2022). Spatiotemporal variation and  
929 provincial scale differences of the AOD across China during 2000–2021. *Atmospheric Pollution*  
930 *Research* 13 (2022) 101359 (14 pp). <https://doi.org/10.1016/j.apr.2022.101359>.

931 de Leeuw, G., Kang, H., Fan, C., Li, Z., Fang, C., Zhang, Y. (2023). Meteorological and anthropogenic  
932 contributions to changes in the Aerosol Optical Depth (AOD) over China during the last decade. *Atm.*  
933 *Env.*, 301, 119676. <https://doi.org/10.1016/j.atmosenv.2023.119676>.

934 Ekman, A. M. L., Eva Nygren, Alejandro Baró Pérez, Matthias Schwarz, Gunilla Svensson, Nicolas  
935 Bellouin.: Influence of horizontal resolution and complexity of aerosol–cloud interactions on marine  
936 stratocumulus and stratocumulus-to-cumulus transition in HadGEM3-GC3.1, *Quart. J Royal Met Soc.*,  
937 149, 755, 2049-2066, <https://doi.org/10.1002/qj.4494>, 2023.

938 Fan J, Wang Y, Rosenfeld D, et al.: Review of aerosol-cloud interactions: Mechanisms, significance, and  
939 challenges. *Journal of the Atmospheric Sciences*,73(11): 4221-4252, 2016.

940 Fan, J., Zhang, Y., Li, Z., Yan, H., Prabhakaran, T., Rosenfeld, D., & Khain, A.: Unveiling aerosol  
941 impacts on deep convective clouds: Scientific concept, modeling, observational analysis, and future  
942 direction, *Journal of Geophysical Research: Atmospheres*, 130, e2024JD041931. [https://doi.org/10.1029/](https://doi.org/10.1029/2024JD041931)  
943 [2024JD041931](https://doi.org/10.1029/2024JD041931), 2025.

944 Feingold, G., Remer, L. A., Ramaprasad, J., Kaufman, Y. J.: Analysis of smoke impact on clouds in  
945 Brazilian biomass burning regions: an extension of Twomey’s approach, *J. Geophys. Res.*, 106 (D19),  
946 22907-22922, 2001.

947 Feingold, G. Modeling of the first indirect effect: analysis of measurement requirements, *Geophys. Res.*  
948 *Lett.*, 30, 1997, doi:10.1029/2003GL017967, 2003.

949 Feingold, G., Goren, T., and Yamaguchi, T.: Quantifying albedo susceptibility biases in shallow clouds,  
950 *Atmos. Chem. Phys.*, 22, 3303–3319, <https://doi.org/10.5194/acp-22-3303-2022>, 2022.

951 Grandey, B.S., Stier, P.: A critical look at spatial scale choices in satellite-based aerosol indirect effect  
952 studies. *Atmos. Chem. Phys.*, 10, 11459-11470, 2010.

953 Gryspeerdt, E., Stier, P., and Partridge, D. G.: Satellite observations of cloud regime development: the  
954 role of aerosol processes, *Atmos. Chem. Phys.*, 14, 1141-1158, doi:10.5194/acp-14-1141-2014, 2014.

955 Gryspeerdt, E., Povey, A. C., Grainger, R. G., Hasekamp, O., Hsu, N. C., Mulcahy, J. P., Sayer, A. M.,  
956 and Sorooshian, A.: Uncertainty in aerosol–cloud radiative forcing is driven by clean conditions, *Atmos.*  
957 *Chem. Phys.*, 23, 4115-4122, <https://doi.org/10.5194/acp-23-4115-2023>, 2023.

958 Gryspeerdt, E., McCoy, D. T., Crosbie, E., Moore, R. H., Nott, G. J., Painemal, D., Small-Griswold, J.,  
959 Sorooshian, A., and Ziemba, L.: The impact of sampling strategy on the cloud droplet number  
960 concentration estimated from satellite data, *Atmos. Meas. Tech.*, 15, 3875–3892, 2022,  
961 <https://doi.org/10.5194/amt-15-3875-2022>, 2022.

962 Glotfelty, T., Kiran Alapaty, Jian He, Patrick Hawbecker, Xiaoliang Song, and Guang Zhang. Studying  
963 Scale Dependency of Aerosol–Cloud Interactions Using Multiscale Cloud Formulations, 77, 11, 2020.

964 Grosvenor, D. P., Sourdeval, O., Zuidema, P., Ackerman, A., Alexandrov, M. D., Bennartz, R., Boers,  
965 R., Cairns, B., Chiu, J. C., Christensen, M., Deneke, H., Diamond, M., Feingold, G., Fridlind, A.,  
966 Hünerbein, A., Knist, C., Kollias, P., Marshak, A., McCoy, D., Merk, D., Painemal, D., Rausch, J.,  
967 Rosenfeld, D., Russchenberg, H., Seifert, P., Sinclair, K., Stier, P., Diedenhoven, B. V., Wendisch, M.,  
968 Werner, F., Wood, R., Zhang, Z., and Quaas, J.: Remote sensing of droplet number concentration in  
969 warm clouds: A review of the current state of knowledge and perspectives, *Rev. Geophys.*, 56, 409–453,  
970 <https://doi.org/10.1029/2017RG000593>, 2018.

971 Han, X., Zhao, B., Lin, Y., Chen, Q., Shi, H., Jiang, Z., et al.: Type-dependent impact of aerosols on  
972 precipitation associated with deep convective cloud over East Asia, *Journal of Geophysical Research:*  
973 *Atmospheres*, 127, e2021JD036127. <https://doi.org/10.1029/2021JD036127>, 2022.

974 Hassan, T., Zhang, K., Li, J., Singh, B., Zhang, S., Wang, H., and Ma, P.: Impacts of spatial heterogeneity  
975 of anthropogenic aerosol emissions in a regionally refined global aerosol–climate model, *Geosci. Model*  
976 *Dev.*, 17, 3507-3532, 2024.

977 Huang, R. J., Zhang, Y. L., Bozzetti, C., et al. High secondary aerosol contribution to particulate pollution  
978 during haze events in China, *Nature*, 514, 218–222, 2014.

979 Jia, H. L., Ma, X. Y., Quaas, J., Yin, Y., Qiu, T.: Is positive correlation between cloud droplet effective  
980 radius and aerosol optical depth over land due to retrieval artifacts or real physical processes?  
981 *Atmospheric Chemistry and Physics*, 19, 13, 8879-8896, 2019.

982 Jia, H., Quaas, J., Gryspeerdt, E., Böhm, C., & Sourdeval, O.: Addressing the difficulties in quantifying  
983 droplet number response to aerosol from satellite observations, *Atmospheric Chemistry and Physics*,  
984 22(11), 7353–7372. <https://doi.org/10.5194/acp-22-7353-2022>, 2022.

985 Jones, T. A., Christopher, S. A., & Quaas, J.: A six year satellite-based assessment of the regional  
986 variations in aerosol indirect effects. *Atmospheric Chemistry and Physics*, 9, 4091, 2009.

987 Koren, I., Kaufman, Y. J., Rosenfeld, D., Remer, L. A., Rudich, Y.: Aerosol invigoration and  
988 restructuring of Atlantic convective clouds. *Geophys. Res. Lett.*, 32 (14), L14828, 2005.

989 Kaufman, Y.J. and Fraser, R.S.: The effect of smoke particles on clouds and climate forcing. *Science*,  
990 1997. 277(5332): p. 1636-1639.

991 Kaufman, Y. J., Remer, L., Tanré, D., Li, R., Kleidman, R., Mattoo, S., Levy, R., Eck, T., Holben, B.,  
992 Ichoku, C., Martins, J., and Koren, I.: A critical examination of the residual cloud contamination and  
993 diurnal sampling effects on MODIS estimates of aerosol over ocean, *IEEE Trans. Geosci. Remote Sens.*,  
994 43, 2886–2897, 2005.

995 Kaufman, Y.J., Remer, L.A., Tanré, D., Li, R.R., Kleidman, R., Mattoo, S., Levy, R.C., Eck, T.F., Holben,  
996 B.N., Ichoku, C., Member, IEEE, Martins, J.V., and Koren, I.: A Critical Examination of the Residual  
997 Cloud Contamination and Diurnal Sampling Effects on MODIS Estimates of Aerosol Over Ocean, *IEEE*  
998 *TRANSACTIONS ON GEOSCIENCE AND REMOTE SENSING*, 43, 12, 2005.

999 Kim, S. W., S. C. Yoon, J. Y. Kim, and S. Y. Kim (2007), Seasonal and monthly variations of columnar  
1000 aerosol optical properties over East Asia determined from multi-year MODIS, LIDAR, and AERONET  
1001 Sun/sky radiometer measurements, *Atmos. Environ.*, 41(8), 1634–1651,  
1002 doi:10.1016/j.atmosenv.2006.10.044.

1003 King, M. D., Tsay, S. C., Platnick, S. E., Wang, M., and Liou, K. N.: Cloud Retrieval Algorithms for  
1004 MODIS: Optical Thickness, Effective Particle Radius, and Thermodynamic Phase, MODIS Algorithm  
1005 Theoretical Basis Document, available at: [http://eosps.nasa.gov/sites/default/files/atbd/atbd\\_mod05.pdf](http://eosps.nasa.gov/sites/default/files/atbd/atbd_mod05.pdf),  
1006 1997.

1007 King, M. D., Menzel, W. P., Kaufman, Y. J., Tanré, D., Gao, B. C., Platnick, S., Ackerman, S. A., Remer,  
1008 L. A., Pincus, R., and Hubanks, P. A.: Cloud and aerosol properties, precipitable water, and profiles of  
1009 temperature and water vapor from MODIS, *IEEE T. Geosci. Remote*, 41, 442–458,  
1010 doi:10.1109/TGRS.2002.808226, 2003.

1011 Lebsock, M., Morrison, H., Gettelman, A.: Microphysical implications of cloud-precipitation covariance  
1012 derived from satellite remote sensing. *Journal of Geophysical Research: Atmosphere*, 118, 6521–6533,  
1013 2013.

1014 Levy, R. C., Mattoo, S., Munchak, L. A., Remer, L. A., Sayer, A. M., Patadia, F., and Hsu, N. C.: The  
1015 Collection 6 MODIS aerosol products over land and ocean, *Atmos. Meas. Tech.*, 6, 2989–3034,  
1016 <https://doi.org/10.5194/amt-6-2989-2013>, 2013.

1017 Levy, R. C., Remer, L. A., Kleidman, R. G., Mattoo, S., Ichoku, C., Kahn, R., and Eck, T. F.: Global  
1018 evaluation of the Collection 5 MODIS dark-target aerosol products over land, *Atmos. Chem. Phys.*, 10,  
1019 10399–10420, doi:10.5194/acp-10-10399-2010, 2010.

1020 Lee, S. S., Donner, L. J., Phillips, V. T. J. Impacts of aerosol chemical composition on microphysics and  
1021 precipitation in deep convection, *Atmospheric Research*, 94, 220–237, 2009.

1022 Lee, H.-H., Zheng, X., Qiu, S., and Wang, Y.: Numerical case study of the aerosol–cloud interactions in  
1023 warm boundary layer clouds over the eastern North Atlantic with an interactive chemistry module, *Atmos.*  
1024 *Chem. Phys.*, 25, 6069–6091, <https://doi.org/10.5194/acp-25-6069-2025>, 2025.

1025 Leung, G. R., Saleeby, S. M., Sokolowsky, G. A., Freeman, S. W., and van den Heever, S. C.: Aerosol–  
1026 cloud impacts on aerosol detrainment and rainout in shallow maritime tropical clouds, *Atmos. Chem.*  
1027 *Phys.*, 23, 5263–5278, <https://doi.org/10.5194/acp-23-5263-2023>, 2023.

1028 Li, G. H., Wang, Y., Zhang, R. Y.: Implementation of a two-moment bulk microphysics scheme to the  
1029 WRF model to investigate aerosol-cloud interaction, *Journal of Geophysical Research-Atmospheres*, 113,  
1030 D15, <https://doi.org/10.1029/2007JD009361>, 2008.

1031 Li, Z., et al.: Aerosol and monsoon climate interactions over Asia, *Rev. Geophys.*, 54, 866–929,  
1032 doi:10.1002/2015RG000500, 2016.

1033 Li, Y., Liu, X., and Cai, H.: Numerical simulation of aerosol concentration effects on cloud droplet size  
1034 spectrum evolutions of warm stratiform clouds in Jiangxi, China, *Atmos. Chem. Phys.*, 24, 13525–13540,  
1035 <https://doi.org/10.5194/acp-24-13525-2024>, 2024.

1036 Liu, Y., Lin, T., Zhang, J., Wang, F., Huang, Y., Wu, X., Ye, H., Zhang, G., Cao, X., and de Leeuw, G.:  
1037 Opposite effects of aerosols and meteorological parameters on warm clouds in two contrasting regions  
1038 over eastern China, *Atmos. Chem. Phys.*, 24, 4651–4673, <https://doi.org/10.5194/acp-24-4651-2024>,  
1039 2024.

1040 Liu, Q., Duan, S. Y., He, Q. S., Chen, Y. H., Zhang, H., Cheng, N. X., Huang, Y. W., Chen, B., Zhan, Q.  
1041 Y., Li, J. Z.: The variability of warm cloud droplet radius induced by aerosols and water vapor in  
1042 Shanghai from MODIS observations, *Atmospheric Research*, 253, 105470, 2021.

1043 Liu, Q., Shen, X., Li, L., et al. Impacts of Aerosol Chemical Composition on Cloud Condensation Nuclei  
1044 (CCN) Activity during Wintertime in Beijing, China. *Remote Sens.*, 15, 4119, 2023.

1045 Liu, T. Q., Liu, Q., Chen, Y. H., Wang, W. C., Zhang, H., Li, D., Sheng, J.: Effect of aerosols on the  
1046 macro- and micro-physical properties of warm clouds in the Beijing-Tianjin-Heibei region. *Science of*  
1047 *the Total Environmen*, 720, 137618, 2020.

1048 Liu, Y., Zhang, J., Zhou, P., Lin, T., Hong, J., Shi, L., Yao, F., Wu, J., Guo, H., and de Leeuw, G.:  
1049 Satellite-based estimate of the variability of warm cloud properties associated with aerosol and  
1050 meteorological conditions, *Atmos. Chem. Phys.*, 18, 18187-18202, [https://doi.org/10.5194/acp-18-](https://doi.org/10.5194/acp-18-18187-2018)  
1051 [18187-2018](https://doi.org/10.5194/acp-18-18187-2018), 2018.

1052 Liu, Y., de Leeuw, G., Kerminen, V.-M., Zhang, J., Zhou, P., Nie, W., Qi, X., Hong, J., Wang, Y., Ding,  
1053 A., Guo, H., Krüger, O., Kulmala, M., and Petäjä, T.: Analysis of aerosol effects on warm clouds over  
1054 the Yangtze River Delta from multi-sensor satellite observations, *Atmos. Chem. Phys.*, 17, 5623-5641,  
1055 <https://doi.org/10.5194/acp-17-5623-2017>, 2017.

1056 Liu, Z., Vaughan, M., Winker, D., Kittaka, C., Getzewich, B., Kuehn, R., Omar, A., Powell, K., Trepte,  
1057 C., and Hostetler, C.: The CALIPSO lidar cloud and aerosol discrimination: Version 2 algorithm and  
1058 initial assessment of performance, *J. Atmos. Ocean. Tech.*, 26, 1198–1213, 2009.

1059 Ma, X., Jia, H., Yu, F., and Quaas, J.: Opposite aerosol index-cloud droplet effective radius correlations  
1060 over major industrial regions and their adjacent oceans, *Geophys. Res. Lett.*, 45, 5771–5778,  
1061 <https://doi.org/10.1029/2018GL077562>, 2018.

1062 Ma, P.-L., P. J. Rasch, M. Wang, H. Wang, S. J. Ghan, R. C. Easter, W. I. Gustafson Jr., X. Liu, Y.  
1063 Zhang, and H.-Y. Ma (2015), How does increasing horizontal resolution in a global climate model

1064 improve the simulation of aerosol-cloud interactions?, *Geophys. Res. Lett.*, 42, 5058–5065,  
1065 doi:10.1002/2015GL064183.

1066 Marchant, B., et al.: MODIS Collection 6 shortwave-derived cloud phase classification algorithm and  
1067 comparisons with CALIOP, *Atmos. Meas. Tech. Discuss.*, 8, 11893–11924, 2015.

1068 Matheson, M. A., Coakley Jr., J. A., and Tahnk, W. R.: Aerosol and cloud property from relationships  
1069 for summer stratiform clouds in the northeastern Atlantic from advanced very high resolution radiometer  
1070 observations, *J. Geophys. Res.*, 110, D24204, doi:10.1029/2005JD006165, 2005.

1071 McComiskey, A., & Feingold, G: The scale problem in quantifying aerosol indirect effects. *Atmospheric  
1072 Chemistry and Physics*, 12, 1031. <https://doi.org/10.5194/acp-12-1031-2012>, 2012.

1073 Meskhidze, N., Nenes, A.: Effects of ocean ecosystem on marine aerosol-cloud interaction. *Adv.  
1074 Meteorol*, doi:10.1155/2010/239808, 2010.

1075 Mohebalhojeh, M., Frederick, S., Riemer, N., & West, M. (2026). A Metric for Quantifying Spatial  
1076 Heterogeneity in Gridded Atmospheric Fields. *Earth and Space Science* (preprint).

1077 Murray-Watson, R. J. and Gryspeerdt, E.: Stability-dependent increases in liquid water with droplet  
1078 number in the Arctic, *Atmos. Chem. Phys.*, 22, 5743–5756, <https://doi.org/10.5194/acp-22-5743-2022>,  
1079 2022.

1080 McComiskey, A., G. Feingold, A. S. Frisch, D. D. Turner, M. A. Miller, J. C. Chiu, Q. Min, and J. A.  
1081 Ogren (2009), Anassessment of aerosol-cloud interactions in marine stratus clouds based on surface  
1082 remote sensing, *J. Geophys. Res.*, 114, D09203,doi:10.1029/2008JD011006.

1083 Platnick, S., et al., MODIS Cloud optical properties: User guide for the Collection 6/6.1 level-2  
1084 MOD06/MYD06 product and associated level-3 data sets. v1.1, July 2018.

1085 Proestakis, E., Amiridis, V., Marinou, E., Georgoulas, A. K., Solomos, S., Kazadzis, S., Chimot, J., Che,  
1086 H., Alexandri, G., Biniotoglou, I., Daskalopoulou, V., Kourtidis, K. A., de Leeuw, G., and van der A, R.  
1087 J.: Nine-year spatial and temporal evolution of desert dust aerosols over South and East Asia as revealed  
1088 by CALIOP, *Atmos. Chem. Phys.*, 18, 1337-1362, <https://doi.org/10.5194/acp-18-1337-2018>, 2018.

1089 Possner A., Zubler, E. M., Lohmann, U., and Schär, C.: The resolution dependence of cloud effects  
1090 and ship-induced aerosol-cloud interactions in marine stratocumulus, *J. Geophys. Res. Atmos.*, 121,  
1091 4810–4829, doi:10.1002/2015JD024685, 2016.

1092 Pandey, S. K., Vinoj, V., Panwar, A.: The short-term variability of aerosols and their impact on cloud  
1093 properties and radiative effect over the Indo-Gangetic Plain. *Atmospheric Pollution Research*, 11, 630-  
1094 638, 2020.

1095 Platnick, S., Meyer, K. G., King, M. D., Wind, G., Amarasinghe, N., Marchant, B., Arnold, G. T., Zhang,  
1096 Z., Hubanks, P. A., Holz, R. E., Yang, P., Ridgway, W. L., Riedi, J.: The MODIS cloud optical and  
1097 microphysical products: Collection 6 updates and examples from Terra and Aqua. *IEEE Trans Geosci*  
1098 *Remote Sens.* Jan;55(1):502-525. doi: 10.1109/TGRS.2016.2610522, 2017.

1099 Quaas, J., Boucher, O., Bellouin, N., Kinne, S.: Satellite-based estimate of the direct and indirect aerosol  
1100 climate forcing, *J. Geophys. Res.*, 113, D05204, doi:10.1029/2007JD008962, 2008.

1101 Quaas, J., Stevens, B., Stier, P., and Lohmann, U.: Interpreting the cloud cover – aerosol optical depth  
1102 relationship found in satellite data using a general circulation model, *Atmos. Chem. Phys.*, 10, 6129-  
1103 6135, <https://doi.org/10.5194/acp-10-6129-2010>, 2010.

1104 Quaas, J., Boucher, O., and Lohmann, U.: Constraining the total aerosol indirect effect in the LMDZ and  
1105 ECHAM4 GCMs using MODIS satellite data, *Atmos. Chem. Phys.*, 6, 947–955,  
1106 <https://doi.org/10.5194/acp-6-947-2006>, 2006.

1107 Quaas, J., Ming, Y., Menon, S., Takemura, T., Wang, M., Penner, J. E., Gettelman, A., Lohmann, U.,  
1108 Bellouin, N., Boucher, O., Sayer, A. M., Thomas, G. E., McComiskey, A., Feingold, G., Hoose, C.,  
1109 Kristjánsson, J. E., Liu, X., Balkanski, Y., Donner, L. J., Ginoux, P. A., Stier, P., Grandey, B., Feichter,  
1110 J., Sednev, I., Bauer, S. E., Koch, D., Grainger, R. G., Kirkevåg, A., Iversen, T., Seland, Ø., Easter, R.,  
1111 Ghan, S. J., Rasch, P. J., Morrison, H., Lamarque, J.-F., Iacono, M. J., Kinne, S., and Schulz, M.: Aerosol  
1112 indirect effects – general circulation model intercomparison and evaluation with satellite data, *Atmos.*  
1113 *Chem. Phys.*, 9, 8697–8717, <https://doi.org/10.5194/acp-9-8697-2009>, 2009.

1114 Rao, S., Dey, S.: Consistent signal of aerosol indirect and semi-direct effect on water clouds in the  
1115 oceanic regions adjacent to the Indian subcontinent. *Atmospheric Research*, 232, 2020.

1116 Remer, L. A., Kaufman, Y. J., Tanre, D., Mattoo, S., Chu, D. A., Martins, J. V., Li, R. R., Ichoku, C.,  
1117 Levy, R. C., Kleidman, R. G., Eck, T. F., Vermote, E., and Holben, B. N.: The MODIS aerosol algorithm,  
1118 products, and validation, *J. Atmos. Sci.*, 62, 947–973, <https://doi.org/10.1175/JAS3385.1>, 2005.

1119 Rosenfeld, D., Zhu, Y. N., Wang, M. H., Zheng, Y. T., Goren, T., Yu, S. C.: Aerosol-driven droplet  
1120 concentrations dominate coverage and water of oceanic low-level clouds, *Science*, 363, 6427, 2019.

1121 Sarna, K. and Russchenberg, H. W. J.: Ground-based remote sensing scheme for monitoring aerosol–  
1122 cloud interactions, *Atmos. Meas. Tech.*, 9, 1039–1050, <https://doi.org/10.5194/amt-9-1039-2016>, 2016.

1123 Saponaro, G., Kolmonen, P., Sogacheva, L., Rodriguez, E., Virtanen, T., de Leeus, G.: Estimates of the  
1124 aerosol indirect effect over the Baltic Sea region derived from 12 years of MODIS observations, *Atmos.*  
1125 *Chem. Phys.*, 17, 3133-3143, 2017.

1126 Stephens, G., Vane, D. G., Boain, R. J., Mace, G. G., Sassen, K., Wang, Z., Illingworth, A. J., O’Connor,  
1127 E. J., Rossow, W. B., Durden, S. L., Miller, S. D., Austin, R. T., Benedetti, A., and Mitrescu, C.: The  
1128 CloudSat Science Team: The CloudSat mission and the A-Train, *B. Am. Meteorol. Soc.*, 83, 1771–1790,  
1129 2002.

1130 Sourdeval, O., Laurent C.-Labonnote, Anthony J. Baran, Johannes Mülmenstädt, Gérard Brogniez.: A  
1131 methodology for simultaneous retrieval of ice and liquid water cloud properties. Part 2: Near-global  
1132 retrievals and evaluation against A-Train products, *Quarterly Journal of the Royal Meteorological*  
1133 *Society*, 142, 701, 3063-3081, 2016.

1134 Sundström, A.-M., Kolmonen, P., Sogacheva, L., and de Leeuw, D.: Aerosol retrievals over China with  
1135 the AATSR dual view algorithm, *Remote Sens. Environ.*, 116, 189–198, 2012.

1136 Theodore L. Anderson, Robert J. Charlson, David M. Winker, John A. Ogren, and Kim Holmén.:  
1137 Mesoscale Variations of Tropospheric Aerosols, *Journal of the Atmospheric Sciences*, 60, 1,  
1138 [https://doi.org/10.1175/1520-0469\(2003\)060<0119:MVOTA>2.0.CO;2](https://doi.org/10.1175/1520-0469(2003)060<0119:MVOTA>2.0.CO;2), 2003.

1139 Tang, J., Wang, P., Mickley, L. J., Xia, X., Liao, H., Yue, X., et al.: Positive relationship between liquid  
1140 cloud droplet effective radius and aerosol optical depth over Eastern China from satellite data.  
1141 *Atmospheric Environment*, 48, 244-253. <https://doi.org/10.1016/j.atmosenv.2013.08.024>, 2014.

1142 Tao, W. K., Chen, J. P., Li, Z., Wang, C. E., Zhang, C. D.: Impact of aerosols on convective clouds and  
1143 precipitation, *Reviews of Geophysics*, 50(2), 2012.

1144 Twomey, S. Pollution and the planetary albedo, *Atmos. Environ.*, 1974, 41, 120-125.

1145 Twomey, S.: The influence of pollution on the shortwave albedo of clouds, *J. Atmos. Sci.* 34(7), 1149-  
1146 1152, 1977.

1147 Wang, F., Guo, J., Zhang, J., Wu, Y., Zhang, X., Deng, M., and Li, X.: Satellite observed aerosol-induced  
1148 variability in warm cloud properties under different meteorological conditions over eastern China, *Atmos.*  
1149 *Environ.*, 48, 122–132, 2014.

1150 Wang, F., Guo, J., Zhang, J., Wu, Y., Zhang, X., Deng, M., Li, X.: Satellite observed aerosol-induced  
1151 variability in warm cloud properties under different meteorological conditions over eastern China, *Atmos.*  
1152 *Environ.*, 84, 122-132, 2014.

1153 Wang, Y., Wang, Y., Song, X., Shang, Y., Zhou, Y., Huang, X., Li, Z.: The impact of particulate pollution  
1154 control on aerosol hygroscopicity and CCN activity in North China, *Environmental Research Letters*, 18,  
1155 074028, 2023.

1156 Winker, D. M., Pelon, J. R., and McCormick, M. P.: The CALIPSO mission: Spaceborne lidar for  
1157 observation of aerosols and clouds, *Proc. SPIE, Lidar Remote Sensing for Industry and Environment*  
1158 *Monitoring III*, 4893, doi:10.1117/12.466539, 2003.

1159 Winker, D. M., Hunt, W. H., and McGill, M. J.: Initial performance assessment of CALIOP, *Geophys.*  
1160 *Res. Lett.*, 34, L19803, doi:10.1029/2007GL030135, 2007.

1161 Winker, D. M., Vaughan, M. A., Omar, A., Hu, Y., Powell, K. A., Liu, Z. Y., Hunt, W. H., Young, S.  
1162 A.: Overview of the CALIPSO Mission and CALIOP Data Processing Algorithms, *Journal of*  
1163 *Atmospheric and Oceanic Technology*, 26 (11), 2310-2323, 2009. doi:10.1175/2009JTECHA1281.1.

1164 Winker, D. M., Pelon, J., Coakley Jr, J. A., Ackerman, S. A., Charlson, R. J., Colarco, P. R., Flamant, P.,  
1165 Fu, Q., Hoff, R. M., Kittaka, C., Kubar, T. L., Le Treut, H., McCormick, M. P., Mégie, G., Poole, L.,  
1166 Powell, K., Trepte, C., Vaughan, M. A., and Wielicki, B. A.: The CALIPSO Mission. *Bulletin of*  
1167 *American Meteorological Society*, 91(9), 1211-1230, 2010.

1168 Wang, F., Guo, J., Zhang, J., Huang, J., Min, M., Chen, T., Liu, H., Deng, M., Li, X.: Multi-sensor  
1169 quantification of aerosol-induced variability in warm clouds over eastern China, *Atmos. Environ.*, 113:  
1170 1-9, 2015. <http://dx.doi.org/10.1016/j.atmosenv.2015.04.063>.

1171 Yuan, T., Li, Z., Zhang, R., and Fan, J.: Increase of cloud droplet size with aerosol optical depth: an  
1172 observation and modeling study, *J. Geophys. Res.*, 113, D04201, doi:10.1029/2007JD008632, 2008.

1173 Zhang, L., Li, J., Li, J., Li, R., Zhang, W., Lei, M., et al.: Studying the impacts of meteorological factors  
1174 on distribution of cloud horizontal scales based on active satellite, *Journal of Geophysical Research:*  
1175 *Atmospheres*, 129, e2024JD041844, <https://doi.org/10.1029/2024JD041844>, 2024.

1176 Zhang, Q., Meng, J., Quan, J., et al. Impact of aerosol composition on cloud condensation nuclei activity,  
1177 *Atmos. Chem. Phys.*, 12, 3783–3790, 2012.

1178 Zhao, J., Ma, X., Quaas, J., and Yang, T.: How meteorological conditions influence aerosol-cloud  
1179 interactions under different pollution regimes, *Atmos. Chem. Phys.*, 25, 17701–17723,  
1180 <https://doi.org/10.5194/acp-25-17701-2025>, 2025.

1181 Zheng, B., Tong, D., Li, M., Liu, F., Hong, C., Geng, G., Li, H., Li, X., Peng, L., Qi, J., Yan, L., Zhang,  
1182 Y., Zhao, H., Zheng, Y., He, K., and Zhang, Q.: Trends in China's anthropogenic emissions since 2010  
1183 as the consequence of clean air actions, *Atmos. Chem. Phys.*, 18, 14095–14111,  
1184 <https://doi.org/10.5194/acp-18-14095-2018>, 2018.

1185 Zheng, X., Dong, X., Xi, B., Logan, T., and Wang, Y.: Distinctive aerosol–cloud–precipitation  
1186 interactions in marine boundary layer clouds from the ACE-ENA and SOCRATES aircraft field  
1187 campaigns, *Atmos. Chem. Phys.*, 24, 10323–10347, <https://doi.org/10.5194/acp-24-10323-2024>, 2024.

1188 Zheng, X., Xi, B., Dong, X., Logan, T., Wang, Y., and Wu, P.: Investigation of aerosol–cloud interactions  
1189 under different absorptive aerosol regimes using Atmospheric Radiation Measurement (ARM) southern  
1190 Great Plains (SGP) ground-based measurements, *Atmos. Chem. Phys.*, 20, 3483–3501,  
1191 <https://doi.org/10.5194/acp-20-3483-2020>, 2020.

1192

1193

1194

1195